Study of defects in Aluminium using large scale electronic structure calculations

by

Balachandran Gadaguntla Radhakrishnan

A dissertation submitted in partial fulfillment
of the requirements for the degree of
Doctor of Philosophy
(Mechanical Engineering)
in the University of Michigan
2014

Doctoral Committee:

Professor Vikram Gavini, Chair
Professor Krishnakumar R Garikipati,
Professor Donald Jason Siegel,
Professor Veera Sundararaghavan

This thesis is dedicated to my parents, friends and
my dear wife

A C K N O W L E D G M E N T S

I would like to thank my advisor, Prof. Vikram Gavini, for giving me the opportunity to perform cutting-edge research. His insight and encouragement have been a constant source of drive in achieving my goals.

I would like to acknowledge Prof. Krishna Garikipati, Prof. Don Siegel, Prof. Veera Sundararaghavan and Prof. Anton Van der Ven for the meaningful discussions that I have had on my thesis work. Their comments and suggestions have always been extremely valuable. I would also like to thank Dr. Jaroslaw Knap of Army research Lab for his kind help in computational aspects of my project.

Dr. Siva Rudraraju, a constant in the mechanical department since I came to Ann Arbor in 2008, has always been very willing to lend a ear and offer advice in trying times. I will always remember all the coffee-walks that we had throughout my stay in Ann Arbor.

I would like to thank my lab-mates: Mrinal, Phani and Ram whose interactions have made my time in the mechanical department enjoyable as well as educative. In particular, I would like to acknowledge Mrinal for his collaborative work in the edge dislocation studies.

My stay in Ann Arbor would have been extremely colorless if not for my friends. I would like to take this opportunity to give a shout-out to them. My roommates: vateez, shiva, one-week-in-a-month roomie dinki have been part of many fun-filled hangouts. My home was always filled with friends who spent more time at home than myself. This includes divya, sardar, shyam, swapnaa, anee, rao-garu, meki, raghu, manix, aarthi, shreya, ram, deepan and shobi. My road trips with these guys was a yearly pilgrimage that I was always looking forward to.

I would like to thank my mom, Lalitha, my dad, Radhakrishnan and my uncle, Chuna, for their constant encouragement. My brother, Prasad, and my sister-in-law, Priya, have been a great source of support throughout my grad-life while master Gautam has been a recent source of entertainment.

Last, but not the least, I would like to thank my wife, Nithya, for her constant support and patience. I met and married her during my grad-life in UM (which made my grad-life even more worthy). She has been a great source of encouragement, especially during days when I needed to hear something positive to keep pushing forward.

TABLE OF CONTENTS

LIST OF FIGURES

Figure

LIST OF TABLES

Table

ABSTRACT

Defects in materials play an important role in determining their behavior. Defects, such as vacancies, dislocations, surfaces, dopants, interstitials, though present in small concentrations of the order of few parts per million (*ppm*), can influence properties of the materials at macroscopic scales. Various computational techniques have been used to model the influence of defects on the properties of materials. Density functional theory based electronic structure calculations have been very accurate in predicting material properties. Electronic structure calculations have provided various insights into the properties of materials such as bulk properties, surface energetics and phase transformations. But, their applicability in studying defect properties is restricted due to limitations on simulation cell-size, to the order of a few hundred to thousand atoms. Recently developed coarse graining technique Quasi Continuum orbital free density functional theory (QCOFDFT) addresses these issues using a real-space local variational formulation of the orbital free density functional theory, finite element discretization of the formulation and an adaptive coarse graining technique. Using this technique, multi-million atom simulations with arbitrary boundary conditions are accessible, which are instrumental in modeling defects in crystalline materials.

In this thesis, we extend the QCOFDFT technique to the more accurate *non-local* kinetic energy functionals that describe materials systems whose electronic structure is close to that of a free electron gas. First, we present a local variational reformulation of the *non-local* functionals. The accuracy of this local formulation is validated with calculations on bulk properties of Aluminium and compared against plane-wave basis implementations. The coarse graining technique, QCOFDFT, is then used with this local reformulation to achieve multi-million atom simulations of vacancies in Aluminium. Cell-size studies are performed on mono and di-vacancies to underscore the need of large scale electronic structure calculations for an accurate understanding of the eneregtics of defects. The real-space formulation is then used to study an isolated edge dislocation to characterize the defect

core and investigate the influence of external deformations on defect-core energetics. Finally, we use QCOFDFT to study vacancy clustering and nucleation of dislocation loops which have important consequences in embrittlement of metals due to radiation damage and quenching processes.

CHAPTER 1

Introduction

Defects in materials play a significant role in influencing a wide range of materials properties. Though present in small concentrations, of the order of few parts per million, defects can influence the properties of materials at macroscopic scales. Examples include the role of vacancies in creep, spalling and ageing, dislocations in metal plasticity, dopants in semiconductor properties, and domain walls in ferroelectric properties [4, 5]. Defects influence the electronic structure close to the defect core which govern the position of nuclei in the nearby vicinity. In addition to the sub-atomic perturbations, defects also create long ranged elastic fields at continuum scales [4]. It is this interaction of multiple length scales that makes the modeling of defects a challenging problem.

Defects can also influence the properties at macroscopic scales through interaction with each other and with external deformations. Interaction of dislocations with solute particles are known to soften or harden the material [6]. Creation of jogs through interaction of dislocations can contribute to work hardening of the materials [5, 7]. Dislocation cores are experimentally observed to behave like sinks attracting vacancies and other interstitials. A complete understanding of such interactions can help in predicting the material behavior as well as design materials with desired properties.

To understand the influence of defects on material properties, a number of quantitative approaches have been used to model the behavior of defects. Continuum theories have been

one of the most widely used techniques in modeling defects. Within the constraints of elastic limit, continuum theories have been successful in predicting the far-field elastic fields created by the defects, but fail close to defect-core. In particular, consider a dislocation in crystalline solids whose elastic strain fields are $O(1/r)$, where r denotes the distance from the dislocation line [5]. Such elastic fields, in addition to having a singularity at the defect-core, predict strains near the defect-core that are never realized in any material. While they have been accurate in predicting the physics far away from the defect-core, close to the defect, quantum mechanical interactions dominate the physics and these can not be described using continuum theories.

Recent surge in the computational capabilities have spurred the development of atomistics based calculations. One of the most widely used computational tools to study material properties from a non-continuum, discrete atomic framework are the interatomic potentials based methods. Interatomic potentials based atomistic calculations have shed light on various phenomenon [8, 9, 10, 11, 12, 13] but they are limited in their applicability in predicting the properties of defects. In particular, the parameters in the interatomic potentials are fit to specific material properties and often are not transferable to the study of other material properties. For example, if the interatomic potential are fit to surface energies, they can capture surface related phenomenon, but may not be able to accurately model grain boundaries. Thus, the applicability of interatomic potentials in uncovering new physics is not considered reliable.

Electronic structure calculations have been one of the most accurate *ab-initio* computational tools in predicting the properties of materials [14]. Electronic structure calculations have provided great insights into various properties of materials including mechanical, electronic, optical and magnetic properties. Further, these theories are transferable and capable of predicting the properties of a wide range of materials. Hartree Fock method and density

functional theory are two of the most widely used electronic structure calculations [15]. In this thesis, we limit ourselves to using density functional theory based methods.

Density functional theory based methods, though computationally tractable compared to solving the Schrödinger's equation, is still computationally expensive and scales as $O(N^3)$ where N denotes the number of electrons in the material system [15, 16]. This has restricted the number of atoms that can be simulated to a few *hundred* atoms. While such cell-sizes are sufficient to predict bulk properties of materials, studies on defects may require much larger cells to understand the complete physics. In addition to the sub-atomic perturbations to the electronic structure, the long ranged electrostatic as well as elastic fields may require much larger cell-sizes. To this end, a number of multi-scale methods were developed. Most of these methods used density functional theory based calculations to compute the physics in small cell-sizes which are then subsequently embedded in coarser models such as interatomic potentials based methods or continuum theories to account for the elastic fields on continuum scales [17, 18]. Such schemes suffered from uncontrolled approximations in embedding the electronic structure calculations in coarser theories whose convergence cannot be systematically ascertained.

Another drawback of the widely available DFT implementations is the inability to consider arbitrary boundary conditions. Most DFT implementations are based on a plane-wave basis which are restricted to periodic boundary conditions on the simulation cell. While this is favorable in calculations of bulk properties, this is a severe restriction in the simulation of defects. In particular, defects such as dislocations produce long-ranged elastic fields that are incompatible with periodic boundary conditions [4]. To overcome this constraint, artificial constructs such as quad-pole construction of dislocations are introduced that are never realized in nature [19, 20].

One promising multi-scale scheme that is devoid of the aforementioned limitations is

the Quasi-Continuum orbital free density functional theory (QCOFDFT) [21]. QCOFDFT is a seamless multi-scale scheme that can be used to perform multi-million atom calculations using orbital free density functional theory as the sole input physics. QCOFDFT is based on

- real-space variational formulation of orbital free density functional theory
- finite element basis
- adaptive coarse graining of the finite element mesh

The quasi-continuum reduction of the orbital free density functional theory was initially implemented for local kinetic energy functionals [21]. Recent advances in modeling of the kinetic energy of the electrons have resulted in more accurate non-local kinetic energy functionals. Such non-local terms cannot be directly implemented in a real-space finite element basis. To this end, in this thesis, a local reformulation of the non-local terms is proposed based on variational principle. This local reformulation is then implemented in the quasi-continuum framework and benchmarked against plane-wave basis implementations. To demonstrate the capabilities of the coarse graining technique, we study the problem of an isolated edge dislocation in aluminium and predict its properties. We also study the mechanism of vacancy clustering in aluminium by studying various sizes of vacancy clusters and predicting their energetics.

The thesis is organized as follows: in the next chapter (Chapter 2), a review of the density functional theory method is presented. In particular, we focus on the orbital free density functional theory. Various efforts that were taken to improve the modeling of the kinetic energy functional are presented including the most recent advances that are being used in this thesis.

In Chapter 3, we present the ideas that are used in the local reformulation of the non-local kinetic energy functionals based on variational formulation. Benchmark calculations of the bulk properties of aluminium are then performed and compared with the plane-wave basis implementations. As a next step in resolving the limits on cell-size, we present the quasi-continuum reduction of the orbital free density functional theory in the context of the non-local kinetic energy functionals. The extension of the quasi-continuum framework to the non-local kinetic energy functionals is verified using mono and di-vacancy studies in aluminium. The cell-size studies performed underscore the need to consider large simulation domains to accurately compute the energetics of defects.

In Chapter 4, we discuss the electronic structure calculations conducted to study an isolated edge dislocation in aluminium. The real-space finite element framework provides the ability to apply arbitrary boundary conditions that are exploited in studying the properties of an isolated dislocation-core. Using the real-space finite element framework, we predict the size of dislocation-core wherein continuum theories are inaccurate and quantum mechanical interactions dominate the energetics. We predict the dislocation-core energy of a full edge dislocation as well as the dissociated Shockley partials. Of particular interest in understanding the behavior of dislocations is the effect of external deformations on the dislocation-core energy. To this end, we study the effect of volumetric deformation on the core-energy of the Shockley partials and estimate the force due to the interaction of dislocation-core with external deformation. Examples are used to demonstrate and calculate this *core-force*.

In Chapter 5, we investigate the mechanism of vacancy clustering and dislocation loops in aluminium. Experimental observations on quenched aluminium specimen have long suspected that vacancies cluster and form dislocation loops on favorable planes. To begin with, we investigate mono-, di- and quad-vacancies and predict their binding energies. Us-

ing experimental observations as a guiding hand, we then investigate symmetric hexagonal vacancy loops on $\{111\}$ plane consisting of 7 and 19 vacancies. In particular, we observe that the plane of atoms above and below the 19 vacancy loop collapses to create a stable dislocation loop with a component of the burger's vector normal to plane of the dislocation loop. This could potentially confirm the long hypothesized mechanism of vacancy clustering in preferential habit planes to create dislocation loops. Finally, we present our conclusions in Chapter 6 and possible future research questions that can be pursued based on the results from this dissertation.

CHAPTER 2

Density Functional Theory: A Review

The non-relativistic time-independent Schrödinger's equation for a material system containing N electrons and M nuclei is given by the eigen-value problem [15]:

$$H\psi = E\psi \tag{2.1}$$

where $\psi(\mathbf{x}_1, \mathbf{x}_2..., \mathbf{x}_N, \mathbf{R}_1, \mathbf{R}_2..., \mathbf{R}_M)$ is the wave function, E is the energy of the system corresponding to the wave function and H is the Hamiltonian of the system. The wave function, $\psi(\mathbf{x}_1, \mathbf{x}_2..., \mathbf{x}_N, \mathbf{R}_1, \mathbf{R}_2..., \mathbf{R}_M)$, belongs to a space of square integrable functions. The argument $\mathbf{x}_i = (\mathbf{r}_i, s_i)$ represents the position $\mathbf{r}_i \in \mathbb{R}^3$, spin s_i of the i^{th} electron and $\mathbf{R}_I \in \mathbb{R}^3$ represents the position of the I^{th} nucleus. The Hamiltonian in 2.1 comprises of the kinetic energy of the electrons, kinetic energy of the nuclei, the interaction between the electrons, electron-nuclei interactions and the nuclei-nuclei repulsion:

$$\begin{aligned} H = &\sum_{i=1}^{N} -\frac{1}{2}\nabla_i^2 + \sum_{I=1}^{M} -\frac{1}{2m_I}\nabla_I^2 + \frac{1}{2}\sum_{i=1}^{N}\sum_{j=1,j\neq i}^{N}\frac{1}{|\mathbf{r}_i - \mathbf{r}_j|} + \sum_{i=1}^{N}\sum_{I=1}^{M}\frac{-\mathbf{Z}_I}{|\mathbf{r}_i - \mathbf{R}_I|} \\ &+ \frac{1}{2}\sum_{I=1}^{M}\sum_{J=1,J\neq I}^{M}\frac{\mathbf{Z}_I\mathbf{Z}_J}{|\mathbf{R}_I - \mathbf{R}_J|} \end{aligned} \tag{2.2}$$

where, m_I is the mass of the I^{th} nucleus relative to the mass of the electrons which is taken to be 1 in *Hartree atomic units*. All the equations in this thesis are expressed in

Hartree atomic units unless otherwise stated explicitly. In general, $\sum_{I=1}^{M} -\frac{1}{2m_I}\nabla_I^2$, the kinetic energy of the nuclei are neglected. As the nuclei are much heavier compared to the the electrons, the kinetic energy of nuclei is much smaller compared to the kinetic energy of electrons and thus neglected. This is called the Born-Oppenheimer approximation [22].

In an N electron system ψ belong to a $3N$ dimensional space, $\psi \in \mathbb{R}^{3N}$. The computational complexity of solving the Schrödinger's equation makes the solution of a general many-electron problem intractable. Hence, over the last 70 years, the focus has been on developing approximate theories for the solution of the Schrödinger's equation, which are commonly referred to as *Electronic structure* calculations. Hartree-Fock method and Density functional theory constitute two of most widely used *Electronic structure calculations* that are based on reasonable approximations that have advanced our understanding of material properties from *first principles* [16]. In this chapter, we present a brief review of density functional theory which forms the basis of the present thesis work.

2.1 Density functional theory

Density functional theory is based on a landmark paper [23], wherein, Hohenberg & Kohn proved two theorems with far-reaching implications. The theorems are stated below and their implications will be discussed in this section.

Theorem 1: For any system of interacting particles in an external potential $V_{ext}(\mathbf{r})$, the electron density is uniquely defined. Conversely, $V_{ext}(\mathbf{r})$ is a unique functional of the electron density, apart from a trivial additive constant.

Theorem 2: A universional functional for the Energy, $E(\rho)$, can be determined in terms

of the electron density. The ground state is a global minimum of this functional.

Starting with the variational form of the Schrödinger's equation, the ground state energy can be obtained as

$$E_0 \leq \langle \psi \left| H \right| \psi \rangle . \tag{2.3}$$

The equality holds only when the wave function is the exact ground state wave function. Using 2.2 and 2.3,

$$E_0 \leq \langle \psi \left| T + V_{ee} + V_{ext} \right| \psi \rangle + E_{zz}, \tag{2.4}$$

where, T denotes the kinetic energy of the electrons, V_{ee} denotes the electrostatic interaction between the electrons, E_{zz} is the electrostatic repulsive energy between the nuclei and V_{ext} is the electrostatic interaction between the electrons and the nuclei. Equation 2.4 can be rewritten as,

$$E_0 \leq \langle \psi \left| T + V_{ee} \right| \psi \rangle + \int \rho \left(\mathbf{r} \right) V_{ext} \left(\mathbf{r} \right) \, \mathrm{d}\mathbf{r} + E_{zz} \tag{2.5}$$

where,

$$\rho \left(\mathbf{r}_1 \right) = \int \left| \psi \left(\mathbf{x}_1, \mathbf{x}_2, ..., \mathbf{x}_N \right) \right|^2 \, \mathrm{d}s_1 \, \mathrm{d}\mathbf{x}_2 \, \mathrm{d}\mathbf{x}_N \tag{2.6}$$

It should be noted that V_{ext} is the only non-universal term in the Hamiltonian that differentiates various N-electron systems [23]. The first theorem of Hohenberg & Kohn shows that this V_{ext} is a unique functional of the ground state electron-density of any system and there exists a one-to-one mapping between them. From the second theorem, Hohenberg-Kohn-Sham functional, F^{HKS}, is defined as

$$F^{HKS}(\rho) = \min_{\psi \to \rho} \langle \psi \left| T + V_{ee} \right| \psi \rangle \tag{2.7}$$

wherein, the minimization is over all admissible wave-functions that give rise to a particular electron-density. Hence the ground state energy can be written as

$$E_0 = \min_{\rho}\{F^{HKS}(\rho) + \int \rho\left(\mathbf{r}\right) V_{ext}\left(\mathbf{r}\right)\, \mathrm{d}\mathbf{r} + E_{zz}\} \tag{2.8}$$

The significance of the above equation lies in the fact that finding the ground state energy of any system is now reduced to solving for $\rho \in H^1(\mathbb{R}^3)$ that minimizes 2.8, whereas, the actual Schrödinger's equation involves solving for the many body wave-function. It should be noted that so far, no approximations have been introduced to the Schrödinger's equation and solving for 2.8 is equivalent to solving 2.1. While the derivations have been without any assumptions, the lack of knowledge of the functional form of F^{HKS} becomes the central problem in predicting the material properties from *first principles*. These theorems, as such, do not provide any probable strategies to determine the functional. It is here that various approximations are made to evaluate F^{HKS} so as to avoid solving the Schrödinger's equation.

F^{HKS} functional is essentially composed of the kinetic energy of the electrons and the electron-electron interactions. While the Hohenberg-Kohn theorems established them as functionals of the electron-density, explicitly evaluating this functional seemed an insurmountable problem. This was overcome by an ingenious approach proposed by Kohn & Sham [24]. Making use of properties of a system of non-interacting electrons in an effective potential, the Hohenberg-Kohn-Sham functional was approximated as

$$F^{HKS}(\rho) = T_s(\rho) + E_H(\rho) + E_{xc}(\rho) \tag{2.9}$$

where, $T_s(\rho)$ is the kinetic energy of non-interacting electrons, $E_H(\rho)$ (Hartree energy) is the classical electrostatic interaction of electrons and $E_{xc}(\rho)$ is the exchange and correlation

energy. In effect, the actual system of electrons were replaced by a set of non-interacting electrons operating in an effective potential. The unknown F^{HKS} is now restricted to modeling the $E_{xc}(\rho)$ term, whose exact functional form is unknown. The exchange and correlation energies are usually approximated using *local density approximation* (LDA) [25, 26] and *generalized gradient approximation* (GGA) functionals [27]. The variational problem in equation 2.8 now reduces to the solution of the single-electron wavefunctions (representing the non-interacting electrons) given by the eigenvalue problem:

$$\left(-\frac{1}{2}\nabla^2 + V_{eff}(\rho;\mathbf{R})\right)\psi_i = \epsilon_i\psi_i, \qquad i = 1, 2, ..., N \tag{2.10}$$

$$\rho = \sum_{i=1}^{N} |\psi_i|^2 \quad V_{eff} = \frac{\partial(E_{ext}+E_H+E_{xc})}{\partial\rho} \tag{2.11}$$

where, ψ_i's are the single-electron wave functions of the non-interacting N-electron system. The wave-functions thus calculated are called the Kohn-Sham orbitals. The system of equations stated above are solved in a self-consistent manner. One starts with a guess value of ρ for which V_{eff} is computed using the equation 2.11. For a given value of V_{eff}, ψ_i's are computed using 2.10. This self-consistent iteration is terminated upon convergence of the calculated electron-density, ρ.

2.2 Orbital free Density functional theory

The Kohn-Sham approach, essentially, reduced the problem of solving for N interacting electrons to solving for N non-interacting electrons in an effective potential. Nevertheless, the computational complexity of solving for the *Kohn-Sham* orbitals (2.10) is $O(N^3)$. The matrix diagonalization and the quantum of data to be stored in each step of the self-consistent scheme incurs huge computational costs. The computational cost of solving

for ψ_i's in a self-consistent scheme restricts the size of the system that can be handled to about thousand atoms. This had spurred a great deal of work in modeling the kinetic energy of electrons, $T_s(\rho)$, giving rise to the *Orbital-free* density functional theory, OFDFT. The basic impetus is to avoid computing the one-electron wave-functions and modeling the kinetic energy of electrons as explicit functionals of electron-density. Such a model will not contain any information regarding the electron-orbitals. Hence the nomenclature, *orbital-free*. Orbital-free density functional theory has been shown to be very accurate for materials whose electron-density contribution is close to that of a free electron gas. This includes metallic systems such as Aluminium and Magnesium [28, 1, 16, 29]. Some work has been done towards modeling the kinetic energy functionals of covalently bonded materials as well [30]. The main advantage offered by *Orbital-free* density functional theory is that the computational cost only linearly increases with respect to the number of electrons in the system. This advantage comes at a cost of loss in accuracy when compared to the *Kohn-Sham* approach. The challenge lies in coming up reasonably accurate models of this kinetic energy functional using various approximations based on ideal case scenarios. In this section, we will look at the approach taken in modeling the kinetic energy, in particular, of metallic systems like Aluminium.

2.2.1 Thomas-Fermi model and the von-Weizsac̈ker correction

One of the earliest functionals modeling the kinetic energy based on a local density approximation is the *Thomas-Fermi* model [31, 32] proposed in 1927. Consider a uniform distribution of electrons, given by ρ_0. The Hamiltonian of such a system is given by:

$$H = -\frac{1}{2}\nabla_i^2 \tag{2.12}$$

Upon imposing periodic conditions on the system, the wave-function is calculated to be $\psi_s = C.e^{(i\mathbf{k}.\mathbf{r})}$. The kinetic energy of the electrons can be shown to be [15]:

$$T_s(\rho_0) = C_F \rho_0^{5/3} V \tag{2.13}$$

where, V is the volume of the domain. This model has been extended to materials with varying electron density using local density approximation and is given by:

$$T_s(\rho) = C_F \int \rho^{5/3}(\mathbf{r})\, \mathrm{d}\mathbf{r} \tag{2.14}$$

where, $C_F = \frac{3}{10}(3\pi^2)^{5/3}$. By construction, the Thomas-Fermi model is exact in capturing the kinetic energy of an uniform electron gas. It should be noted that the kinetic energy is treated by considering the *local* electron-density and integrated over the system even for an inhomogeneous system of electrons. Such an approach is called the *local density approximation* which is used to derive the exchange energy as well [25].

While the Thomas-Fermi model gives a simple way to model the kinetic energy of electrons, it has some major drawbacks. The most debilitating of these drawbacks is the inability to predict binding in molecules. Essentially, the Thomas-Fermi model predicted that the atoms are energetically more stable if they are infinitely separated than coming together to form molecules. This was analytically proved by Teller [33] and later on, rigorously shown in the works of Balázs, Lieb and Simon [34, 35, 36]. This proof is generally referred to as *Teller nonbinding theorem*. Most models that were developed later, use the Thomas-Fermi model as the back-bone to which corrections are added to make them more accurate.

The most widely used correction to the Thomas-Fermi model is the von-Weizsac̈ker term. The von-Weizsac̈ker term was developed as the kinetic energy model for single-

orbital systems: one or two electron systems. The Thomas-Fermi-Weizsaćker (TFvW) model is given as:

$$T_s(\rho) = C_F \int \rho^{5/3}(\mathbf{r})\,\mathrm{d}\mathbf{r} + \frac{\lambda}{8}\int \frac{|\nabla\rho(\mathbf{r})|^2}{\rho(\mathbf{r})}\,\mathrm{d}\mathbf{r} \tag{2.15}$$

where λ is a numerical parameter that is empirically fixed to fit the material properties. In the uniform gas limit, the TFvW model reverts to the Thomas-Fermi limit. While the Thomas-Fermi model predicted algebraic decay of electron-density in atoms, the von-Weizsaćker term correctly predicts exponential decay. Most importantly, the TFvW model can predict binding in molecules. The parameter λ plays an important role in the energetics predicted by the TFvW model. Most widely used values of λ are 1, $\frac{1}{9}$ and $\frac{1}{5}$ [37]. Of these values, empirical tests show that $\lambda = \frac{1}{5}$ gives the most favorable energetics of atoms and molecules [38, 39, 37].

2.2.2 Linear Response theory

Consider a system of electrons in their ground state with an external potential V_{ext} and electron density ρ. A perturbation ΔV_{ext} is applied and the perturbation in electron density, $\Delta\rho$ is given by [15]:

$$\Delta\rho(\mathbf{r}) = \int \chi_e(\mathbf{r},\mathbf{r}')\Delta V_{ext}(\mathbf{r}')\,\mathrm{d}\mathbf{r}' + O\left[(\Delta V_{ext})^2\right] \tag{2.16}$$

where $\chi_e(\mathbf{r},\mathbf{r}')$ is the *density response function*. If the external potential changes by a constant throughout the domain, there will be no change induced in the electron density as

$$\int \chi_e(\mathbf{r},\mathbf{r}')\,\mathrm{d}\mathbf{r}' = 0\,. \tag{2.17}$$

Linear response theory is concerned with the properties of this density response function and its implications in electronic structure calculations.

It can be shown from the expansion of energy functional (2.8) that [15],

$$-\chi_e(\mathbf{r},\mathbf{r}')^{-1} = \frac{\delta^2 T_s}{\delta\rho(\mathbf{r})\rho(\mathbf{r}')} + \frac{1}{|\mathbf{r}-\mathbf{r}'|} + \frac{\delta^2 E_{xc}}{\delta\rho(\mathbf{r})\rho(\mathbf{r}')} \tag{2.18}$$

As can be seen from this expression, the response function is directly related to the second order variational derivative of the density functional. The part of this response function that is of interest to us is the contribution from the non-interacting kinetic energy functional, given by

$$-\chi_s(\mathbf{r},\mathbf{r}')^{-1} = \frac{\delta^2 T_s}{\delta\rho(\mathbf{r})\rho(\mathbf{r}')} \tag{2.19}$$

where, $\chi_s(\mathbf{r},\mathbf{r}')$ is called the non-interacting response function. Different systems can have different response functions and it is generally expressed as a function of electron-density. Of particular interest is the response function for a uniformly distributed electron gas which can be derived theoretically. In Fourier space, this response function is given by,

$$\chi_{LR}(q) = -\frac{k_F}{\pi^2}\left[\frac{1}{2} + \frac{4k_F^2 - q^2}{8k_F q}\ln\left|\frac{2k_F+q}{2k_F-q}\right|\right] \tag{2.20}$$

where, $k_F = (3\pi^2\rho)^{1/3}$ is the radius of the *Fermi sphere*. The response function for this special case is called the Lindhard's response function [40]. Realizing that the electron-density distribution of metals like Aluminium, Magnesium etc., are close to that of a free-electron gas, the response function of 2.20 has been used as the benchmark response function of kinetic energy functionals designed to model these metallic systems. In this overview, we will discuss two such classes of kinetic energy functionals: density-independent and density-dependent kernel kinetic energy functionals.

2.2.3 Density independent kinetic energy functionals

We have seen that, by construction, the Thomas-Fermi functional is exact for a uniform distribution of electron gas and the von-Weizsaćker term is exact for a single orbital system. While these class of functionals have shown to be quite accurate for certain scenarios, they do not satisfy the linear response behavior of uniform electron gas subject to perturbations of external potential. One way to develop kinetic energy functionals that satisfy the Lindhard's response function is to explicitly enforce the condition:

$$\hat{F}\left(\frac{\delta^2 T_s}{\delta\rho(\mathbf{r})\delta\rho(\mathbf{r}')}\right) = -\frac{1}{\chi_s}. \tag{2.21}$$

A number of non-local kinetic energy functionals have the form [29, 1]

$$T_s\left(\rho\right) = T_{TF}\left(\rho\right) + T_{vW}\left(\rho\right) + T_X^{\alpha,\beta}\left(\rho\right). \tag{2.22}$$

wherein, the general functional form of $T_X^{\alpha,\beta}\left(\rho\right)$ is given by,

$$T_X^{\alpha,\beta}\left(\rho\right) = C_{TF}\int\int \rho^{\alpha}(\mathbf{r}) K\left(|\mathbf{r}-\mathbf{r}'|\right)\rho^{\beta}(\mathbf{r})\,\mathrm{d}\mathbf{r}\,\mathrm{d}\mathbf{r}'. \tag{2.23}$$

In the above equation 2.23, X denotes various models, α and β are positive parameters. The parameters and the kernel function K are modeled such that the kinetic energy functional in equation 2.22 satisfies the response function in equation 2.21. Table 3.1 shows some of the prominent kinetic energy functionals that were developed based on this model.

It should be noted that the kernel function, K, is density independent by choice thus creating the family of density independent kinetic energy functionals. While these functionals were successful in reproducing the exact linear response function of the kinetic energy functional of a uniform electron gas, their accuracy in capturing defect energetics

Table 2.1: Density Independent kinetic energy functionals

Kinetic Energy Functional (X)	α, β
Wang-Teter-Perrot [41, 42]	$\frac{5}{6}, \frac{5}{6}$
Smargiassi-Madden [43]	$\frac{1}{2}, \frac{1}{2}$
Perrot [41]	$1, 1$
Wang-Teter [42]	$\frac{5}{6} \pm \frac{4\sqrt{2}-5}{6}$
Wang-Govind-Carter [1]	Various values

needed more improvements.

2.2.4 Density dependent kinetic energy functionals

The density independent kernels, while satisfying the linear response function (2.20), were heavily dependent on the parameter value of α. In particular, the mono-vacancy formation energy of Aluminium on which most of these models are tested were inaccurate. Hence, there was a need to come up with a more accurate kinetic energy functional. One of the most accurate kinetic energy functionals recently developed is the density-dependent Wang-Govind-Carter (WGC-DD) [29] kinetic energy functional. The WGC-DD kernel has the functional form

$$T_s^{\alpha,\beta}(\rho) = T_{TF}(\rho) + T_{vW}(\rho) + T_Z^{\alpha,\beta}(\rho) \tag{2.24}$$

wherein, the first two components of the kinetic energy functional are the *Thomas-Fermi* functional and the *von Weizsaäcker* correction. The last term is given by

$$T_Z^{\alpha,\beta}(\rho) = C_{TF} \int \int \rho^{\alpha}(\mathbf{r}) K\left[\xi_{\gamma}(\mathbf{r}, \mathbf{r}'), |\mathbf{r} - \mathbf{r}'|\right] \rho^{\beta}(\mathbf{r}') \, \mathrm{d}\mathbf{r} \, \mathrm{d}\mathbf{r}' \tag{2.25}$$

wherein,

$$\xi_{\gamma}(\mathbf{r}, \mathbf{r}') = \left(\frac{k_F^{\gamma}(\mathbf{r}) + k_F^{\gamma}(\mathbf{r}')}{2} \right)^{1/\gamma} \tag{2.26}$$

$$k_F(\mathbf{r}) = \left(3\pi^2\rho(\mathbf{r})\right)^{1/3} \tag{2.27}$$

$k_F(\mathbf{r})$ and $\xi_\gamma(\mathbf{r},\mathbf{r}')$ represent the local one-body and non local two-body *Fermi* wave vectors respectively. Following an approach similar to the density-independent kernels, wherein the parameters in the response function of the kinetic energy functionals are chosen to match the Lindhard's response function, the parameters α, β, γ are determined. A number of combinations were found that can satisfy 2.20. Of these values, the combination that has been widely used and empirically shown to be most accurate is given by $\{\alpha,\beta,\gamma\} = \{\frac{5}{6} \pm \sqrt{5/6}, 2.7\}$.

While the full functional form of the density dependent kernel is given by the equation 2.25, it is never implemented in this form due to the computational complexity involved in calculating the density dependent kernel function, $K[\xi_\gamma(\mathbf{r},\mathbf{r}'), |\mathbf{r}-\mathbf{r}'|]$. Instead, the density dependent kernel is Taylor expanded in terms of density-independent kernels around a reference electron-density, ρ^*. The Taylor series up to second order is given as:

$$\begin{aligned} K[\xi_\gamma(\mathbf{r},\mathbf{r}'), |\mathbf{r}-\mathbf{r}'|] =& K(k_F^*, |\mathbf{r}-\mathbf{r}'|) + \left.\frac{\partial K[\xi_\gamma(\mathbf{r},\mathbf{r}'), |\mathbf{r}-\mathbf{r}'|]}{\partial\rho(\mathbf{r})}\right|_{\rho^*} \Delta\rho(\mathbf{r}) \\ &+ \left.\frac{\partial K[\xi_\gamma(\mathbf{r},\mathbf{r}'), |\mathbf{r}-\mathbf{r}'|]}{\partial\rho(\mathbf{r}')}\right|_{\rho^*} \Delta\rho(\mathbf{r}') \\ &+ \left.\frac{\partial^2 K[\xi_\gamma(\mathbf{r},\mathbf{r}'), |\mathbf{r}-\mathbf{r}'|]}{\partial\rho^2(\mathbf{r})}\right|_{\rho^*} \frac{\Delta\rho(\mathbf{r})^2}{2} \\ &+ \left.\frac{\partial^2 K[\xi_\gamma(\mathbf{r},\mathbf{r}'), |\mathbf{r}-\mathbf{r}'|]}{\partial\rho^2(\mathbf{r}')}\right|_{\rho^*} \frac{\Delta\rho(\mathbf{r}')^2}{2} \\ &+ \left.\frac{\partial^2 K[\xi_\gamma(\mathbf{r},\mathbf{r}'), |\mathbf{r}-\mathbf{r}'|]}{\partial\rho(\mathbf{r})\partial\rho(\mathbf{r}')}\right|_{\rho^*} \Delta\rho(\mathbf{r})\Delta\rho(\mathbf{r}') \end{aligned} \tag{2.28}$$

The functional forms of the first and second order derivatives are readily available and are easier to handle using Fast Fourier Transforms (FFT). Nevertheless, evaluating the density dependent kinetic energy functionals incur huge computational cost, consuming

as much as 60% of the total computational cost of solving the problem [44]. Nevertheless, *Orbital free* density functional theory calculations are computationally less expensive compared to the *Kohn-Sham* implementation while offering nearly comparable accuracy for certain restricted class of materials.

2.3 Summary

In this chapter, we described the basic fundamentals of density functional theory based electronic structure calculations. In particular, we presented the principles based on which kinetic energy functionals are modeled in an *orbital free* density functional theory framework. The available kinetic energy functionals are mostly used in modeling materials whose electronic density is close to that of a free electron gas. In orbital free density functional theory, the problem of finding the ground state energy is now reduced to a minimization of an energy functional with respect to electron density, $\rho \in H^1(\mathbb{R}^3)$ which is computationally tractable. In the next chapter, we will discuss the implementation aspects of this variational problem. In particular, we will focus on the plane-wave basis used to discretize the problem and discuss why a real-space basis can offer significant advantages.

CHAPTER 3

Real space formulation and coarse graining of *Orbital free* density functional theory

In the previous chapter 2, we presented the basic concepts in density functional theory and the approximations involved in the *Orbital free* density functional theory. Also, we presented various models of the kinetic energy functional that were used in *Orbital free* density functional theory. In particular, we focused on the non-local kinetic energy functionals that will be used in this work. In this chapter, we will focus on the implementation of *Orbital free* density functional theory.

Orbital free density functional theory is a linear scaling method $(O[N])$ that has been very accurate in predicting the property of materials whose electron density distribution is close to that of a free electron gas. This includes metallic systems like Aluminium, Sodium, Magnesium etc [28, 1, 16, 29]. *Orbital free* density functional theory has been historically implemented in plane-wave basis numerical schemes [44]. This has been the case due to certain advantages offered by the plane-wave basis which make them very amenable in predicting bulk properties of the material system. But, the use of plane-wave basis also imposes restrictions on the boundary conditions that can be applied. In this chapter, we will present the key ideas exploited in numerical implementation of the *Orbital free* density functional theory. We will focus on the drawbacks of the popular plane-wave basis implementation of *Orbital free* density functional theory and also present key ideas that

we have used in overcoming these restrictions. To this end, we first present a local variational formulation of the *Orbital free* density functional theory energy functional. This is achieved by reformulation of all the extended terms of the energy functional into local formulations based on variational principles. As a next step in realizing the ability to apply arbitrary boundary conditions, we present a real-space implementation based on finite element discretization.

Most implementations of electronic structure calculations are restricted from a few hundred to a thousand atom systems. Plane-wave basis implementations have been very successful in predicting the bulk properties of materials and certain defect properties such as surfaces. But their accuracy in predicting defect properties, in general, are restricted due to limitations on cell-size as well as necessity to apply periodic boundary conditions. One example is dislocations in materials whose elastic strain fields decay as $1/r$, where r is the distance from the defect-core [5] and these displacement fields are incompatible with periodic boundary conditions. To be able to capture the long ranged fields, we need to perform electronic structure calculations at macroscopic scales. To this end, we present coarse graining techniques that can make accessible cell-sizes corresponding to millions of atoms. The coarse graining techniques were previously developed in the context of local kinetic energy functionals [21]. Here, we present ideas to extend them to any class of non-local kinetic energy functionals. Using these ideas, we perform mono and di-vacancy studies and demonstrate the need for large cell-sizes to accurately predict the energetics of defects.

3.1 *Orbital free* density functional theory

The *Orbital free* density functional theory energy functional is given as [16, 15]:

$$E(u, \mathbf{R}) = T_S(u) + E_{XC}(u) + E_H(u) + E_{ext}(u, \mathbf{R}) + E_{ZZ}(\mathbf{R}) \tag{3.1}$$

where $u = \sqrt{\rho}$ is the square root of ground-state electron-density; $\mathbf{R} = \{\mathbf{R}_1, ..., \mathbf{R}_M\}$ is the collection of nuclear positions in the system; T_S is the kinetic energy of non-interacting electrons; E_{XC} denotes the exchange correlation energy; E_H is the classical electrostatic interaction energy between electrons, also referred to as Hartree energy; E_{ext} is the interaction energy of electrons with external field induced by nuclear charges; and E_{ZZ} denotes the repulsive interactions between nuclei. The kinetic energy functional considered here is given by

$$T_S(u) = C_F \int_\Omega u^{10/3}\, \mathrm{d}\mathbf{r} + \frac{1}{2}\int_\Omega |\nabla u(\mathbf{r})|^2\, \mathrm{d}\mathbf{r} + T_K(u) \tag{3.2}$$

where, Ω contains the support of $u(\mathbf{r})$ (the region where $u(\mathbf{r})$ is non-zero). The first two terms in equation 3.2 are the Thomas-Fermi-Weizacker family of orbital-free kinetic energy functionals [16]. The third term corresponds to kernel functionals [1, 29], which were discussed in chapter 2. In this work, the exchange-correlation term has been modelled using the Local Density Approximation (LDA) [45, 46],

$$E_{XC}(u) = \int_\Omega \epsilon_{xc}(u(\mathbf{r}))\, u^2(\mathbf{r})\, \mathrm{d}\mathbf{r} \tag{3.3}$$

where, $\epsilon_{xc} = \epsilon_x + \epsilon_c$ is the exchange and correlation potential given by

$$\epsilon_x = -\frac{3}{4}\left(\frac{3}{\pi}\right)^{1/3} u^{2/3}(\mathbf{r}) \tag{3.4}$$

$$\epsilon_c = \begin{cases} \frac{\gamma}{1+\beta_1\sqrt{r_s}+\beta_2 r_s} & r_s \geq 1 \\ A\log r_s + B + Cr_s \log r_s + Dr_s & r_s < 1 \end{cases} \tag{3.5}$$

where $r_s = \left(\frac{3}{4\pi u^2}\right)^{1/3}$. The values of the constants are determined by whether the system is polarized or unpolarized. We use the constants corresponding to the unpolarized system given by [46] $\gamma_u = -0.1471$, $\beta_{1u} = 1.1581$, $\beta_{2u} = 0.3446$, $A_u = 0.0311$, $B_u = -0.048$, $C_u = 0.0014$, $D_u = -0.0108$.

The last three terms in equation 3.2 represent the electro-static interactions between the electrons and the nuclei in the system:

$$E_H(u) = \frac{1}{2}\int_\Omega \int_\Omega \frac{u^2(\mathbf{r})\, u^2(\mathbf{r}')}{|\mathbf{r}-\mathbf{r}'|}\, \mathrm{d}\mathbf{r}\, \mathrm{d}\mathbf{r}' \tag{3.6}$$

$$E_{ext}(u, \mathbf{R}) = \int_\Omega u^2(\mathbf{r})\, V_{ext}(\mathbf{r}, \mathbf{R})\ \mathrm{d}\mathbf{r} \tag{3.7}$$

$$E_{zz}(\mathbf{R}) = \frac{1}{2}\sum_{I=1}^{M}\sum_{J=1, J\neq I}^{M} \frac{Z_I Z_J}{|\mathbf{R}_I - \mathbf{R}_J|} \tag{3.8}$$

We note that the above expressions are for a non-periodic system. For the periodic system, one of the integral and summation will be over all space. The convolution sums and integrals lend themselves to be easily evaluated using plane-wave basis and *fast Fourier transforms* (FFT). The forward FFT of a function is given by:

$$\hat{F}(f(\mathbf{r})) = \tilde{f}(\mathbf{g}) = \frac{1}{N}\sum_{\mathbf{r}} f(\mathbf{r})\, e^{-i\mathbf{g}.\mathbf{r}} \tag{3.9}$$

To give an example of how the convolution terms are evaluated in Fourier space, let us look

at how the Hartree term, E_H, is evaluated. It is computed as [44]:

$$E_H = \frac{\Omega}{2N} \sum_{\mathbf{r}} \frac{\delta E_H}{\delta \rho} (\mathbf{r}) \, \rho (\mathbf{r}) \tag{3.10}$$

wherein, the potential $\frac{\delta E_H}{\delta \rho} (\mathbf{r})$ is computed using inverse FFTs as:

$$\frac{\delta E_H}{\delta \rho} (\mathbf{r}) = \hat{F}' \left(\frac{4\pi}{|\mathbf{g}|^2} \tilde{\rho} (\mathbf{g}) \right) \tag{3.11}$$

wherein, $\tilde{\rho} (\mathbf{g})$ is the FFT of $\rho (\mathbf{r})$ obtained using 3.9. $\hat{F}'$ represents the inverse FFT given by:

$$\hat{F}' (f (\mathbf{g})) = f (\mathbf{r}) = \sum_{\mathbf{g}} f (\mathbf{g}) \, e^{i \mathbf{g} . \mathbf{r}} \tag{3.12}$$

Importantly, the Fourier transform of two convolving functions is the product of the Fourier transforms of the two functions. This feature has been exploited in all popular implementations of electronic structure calculations. But, the use of plane-wave basis can be restrictive as well. Periodic boundary conditions *have* to be applied on the simulation cell. This requirement on the simulation cells is advantageous while performing bulk property studies like predicting the elastic constants, stacking fault energies etc. But, this becomes disadvantageous when arbitrary boundary conditions based on long-ranged elastic fields need to applied. Also, use of Fourier transforms hinder the scalability in parallel implementations. The plane-wave basis set also requires uniform discretization which is not efficient in the study of defects, which require higher resolution near the defect-core, but a coarser resolution suffices elsewhere. These aforementioned restrictions often limit the size of systems that can be considered to a few thousand atoms. In this chapter, we will present the ideas that pave way for application of arbitrary boundary conditions and enable the consideration of multi-million atom simulation cells. To this end, we present real-space formulation

based on variational principles in the next section.

3.2 Real-space formulation

In order to address the prior discussed limitations of a plane-wave discretization, a number of efforts have been directed towards the implementation of OFDFT in real-space [47, 48]. The most popular real-space implementations are either based on the Finite difference method or the Finite element method. The finite difference implementation in general employs a uniform discretization of the domain. Though the finite difference method uses real-space discretization in [47], the convolution integrals of electron-electron interaction and the non local terms of the kinetic energy functional are evaluated using *FFT*s. This, as we have already seen in the case of plane-wave basis implementations, limits scalability in parallel implementations. In general, one advantage of the finite difference implementation over Fourier space implementation is the ability to apply non-periodic boundary conditions. A detailed discussion on the finite difference implementation of orbital free density functional theory can be found in [47]. While the finite difference implementation is not restricted to periodic boundary conditions, it still limits the system sizes due to uniform discretization. It is here that the finite element implementation offers features that are amenable to achieving large scale electronic structure calculation with arbitrary boundary conditions.

Of the terms in the OFDFT energy functional (3.1), the electrostatic interactions and the non-local component of the kinetic energy functionals are extended in real-space. Here, we seek to re-write them in a local form based on variational principle. To this end, the point charges Z_I at R_I are regularized with a smooth function $Z_I\delta_{R_I}(\mathbf{r})$ which has a small support radius around R_I and a total charge of Z_I [48]. We can re-write the nuclear inter-

actions, E_{zz}, as

$$E_{zz} = \frac{1}{2}\int_{\Omega}\int_{\Omega} \frac{b\left(\mathbf{r}\right) b\left(\mathbf{r}'\right)}{|\mathbf{r}-\mathbf{r}'|}\,\mathrm{d}\mathbf{r}\,\mathrm{d}\mathbf{r}' \tag{3.13}$$

where, $b\left(\mathbf{r}\right) = \sum_{I=1}^{M} Z_I \delta_{R_I}\left(\mathbf{r}\right)$. It should be noted that this functional differs from the previous summation based evaluation of E_{zz} by the self-energy of the nucleus which is an inconsequential constant. This constant can be evaluated precisely and subtracted from the energy functional [49].

The electrostatic interactions in the system can now be rewritten in the variational form:

$$J_{\phi} = \sup_{\phi}\left\{-\frac{1}{8\pi}\int \left|\nabla\phi\left(\mathbf{r}\right)\right|^2 \,\mathrm{d}\mathbf{r} + \int \left(u^2\left(\mathbf{r}\right) + b\left(\mathbf{r}\right)\right)\phi\left(\mathbf{r}\right)\,\mathrm{d}\mathbf{r}\right\} \tag{3.14}$$

where,

$$J_{\phi} = E_{zz} + E_H + E_{ext} \tag{3.15}$$

We note that the Euler-Lagrange equation associated with the above variational form of electrostatic interactions is given by:

$$-\frac{1}{4\pi}\Delta\phi = u^2 + b, \tag{3.16}$$

where,

$$\phi\left(\mathbf{r}\right) = \int_{\Omega} \frac{b\left(\mathbf{r}'\right)}{|\mathbf{r}-\mathbf{r}'|}\,\mathrm{d}\mathbf{r}' + \int_{\Omega} \frac{u^2\left(\mathbf{r}'\right)}{|\mathbf{r}-\mathbf{r}'|}\,\mathrm{d}\mathbf{r}' \tag{3.17}$$

This local reformulation of the electrostatic interactions was developed in Ref. [48]

The other non-local term is the kinetic energy functional. The non-local kernel kinetic energy functionals were designed to be easily implemented in plane-wave basis. More detailed discussion of these classes of kinetic energy functionals can be found in Chapter 2. Here, we seek to derive a local reformulation of these functionals in real-space based on

variational principles. We implement this local reformulation based on the ideas developed in Ref. [2]. We restrict ourselves to the Wang-Govind-Carter density independent (WGC-DI) [1] and density dependent (WGC-DD) [29] kinetic energy functionals as they have evolved into the most accurate kinetic energy functionals available till date. First, we present the ideas in the context of the WGC-DI kinetic energy functionals. The extension to the WGC-DD kinetic energy functionals will be discussed subsequently.

The WGC-DI kinetic energy functional can be written as

$$T_K\left(u\left(\mathbf{r}\right)\right) = \int\int u^{2\alpha}\left(\mathbf{r}\right) K\left(\left|\mathbf{r}-\mathbf{r}'\right|\right) u^{2\beta}\left(\mathbf{r}'\right)\, \mathrm{d}\mathbf{r}\, \mathrm{d}\mathbf{r}' \tag{3.18}$$

Introducing the following potentials

$$V_\alpha\left(\mathbf{r}\right) = \int K\left(\left|\mathbf{r}-\mathbf{r}'\right|\right) u^{2\alpha}\left(\mathbf{r}'\right)\, \mathrm{d}\mathbf{r}', \tag{3.19}$$

$$V_\beta\left(\mathbf{r}\right) = \int K\left(\left|\mathbf{r}-\mathbf{r}'\right|\right) u^{2\beta}\left(\mathbf{r}'\right)\, \mathrm{d}\mathbf{r}', \tag{3.20}$$

the kinetic energy functional can be evaluated, either as

$$T_K\left(u\left(\mathbf{r}\right)\right) = \int V_\beta\left(\mathbf{r}\right) u^{2\alpha}\left(\mathbf{r}\right)\, \mathrm{d}\mathbf{r}, \tag{3.21}$$

or as:

$$T_K\left(u\left(\mathbf{r}\right)\right) = \int V_\alpha\left(\mathbf{r}\right) u^{2\beta}\left(\mathbf{r}\right)\, \mathrm{d}\mathbf{r}. \tag{3.22}$$

The potentials in Fourier space can be evaluated as:

$$\hat{V}_\alpha\left(q\right) = \hat{K}\left(q\right) \widehat{u^{2\alpha}}\left(q\right) \tag{3.23}$$

$$\hat{V}_\beta\left(q\right) = \hat{K}\left(q\right) \widehat{u^{2\beta}}\left(q\right) \tag{3.24}$$

The functional form of the kernel, $K\left(|\mathbf{r}-\mathbf{r}'|\right)$, in Fourier space is given as [1]

$$\hat{K}\left(q\right)=-\frac{k_F}{\pi^2\chi_{LR}\left(q\right)}-1-3q^2. \tag{3.25}$$

The functional form of the kernel function in Fourier-space is shown in figure 3.1. In order

Figure 3.1: Kernel function in Fourier-space [1]

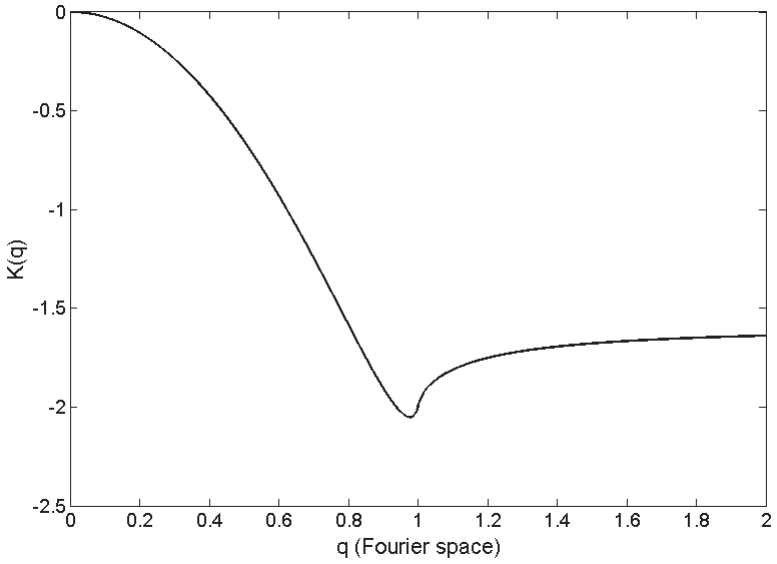

to implement the WGC family of kinetic functionals in real-space, we consider approximating $\hat{K}\left(q\right)$ in Fourier space using rational functions as follows [2]:

$$\tilde{K}\left(q\right)=\sum_{j=1}^{m}\frac{A_j q^2}{B_j+q^2} \tag{3.26}$$

where, A_j and B_j are complex coefficients that are determined using the best fit approximation. The number of terms in the summation can be systematically increased to get more accurate fits. The fit parameters are listed below in the table 3.1.

Figure 3.2: Complex polynomial fit to the kernel function [2]

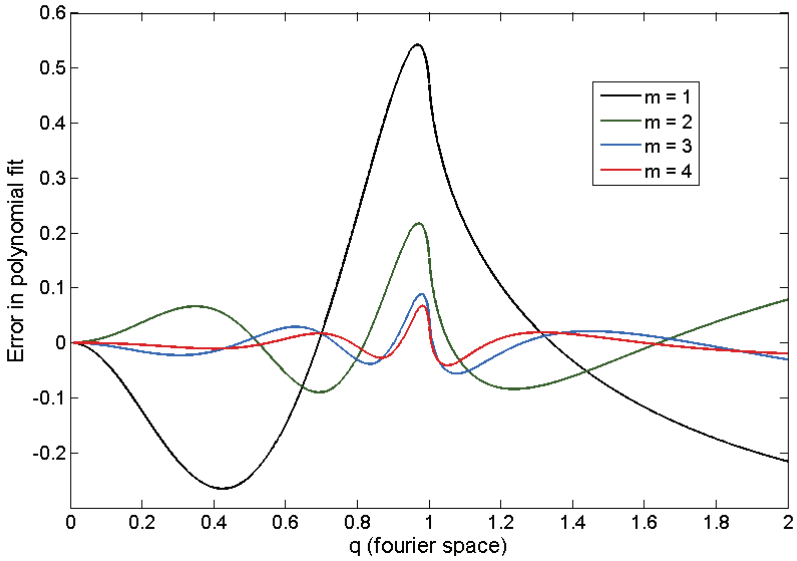

Table 3.1: Optimized fitting parameters for the $K(q)$ with an order eight $(m = 4)$ rational function. The parameters for even indices are complex conjugates of those of the odd indices [2]

	$j = 1$	$j = 3$
A_j	$0.026696 + i0.145493$	$-0.826696 + i0.691930$
B_j	$-0.818245 - i0.370856$	$0.343051 - i0.689646$

We now define the following potentials:

$$\hat{V}_{\alpha_j}(q) = \frac{A_j q^2}{B_j + q^2} \widehat{u^{2\alpha}}(q) \qquad j = 1, ..., m$$

$$\hat{V}_{\beta_j}(q) = \frac{A_j q^2}{B_j + q^2} \widehat{u^{2\beta}}(q) \qquad j = 1, ..., m \tag{3.27}$$

Taking the inverse Fourier transform of the above equations 3.27, we obtain a system of Helmholtz equations given by

$$-\nabla^2 V_{\alpha_j}(\mathbf{r}) + B_j V_{\alpha_j}(\mathbf{r}) + A_j \nabla^2 u^{2\alpha}(\mathbf{r}) = 0 \qquad j = 1, ..., m$$

$$-\nabla^2 V_{\beta_j}(\mathbf{r}) + B_j V_{\beta_j}(\mathbf{r}) + A_j \nabla^2 u^{2\beta}(\mathbf{r}) = 0 \qquad j = 1, ..., m \tag{3.28}$$

Under the approximation given by Eq. 3.26, the potentials now reduce to $V_\alpha(\mathbf{r}) = \sum_{j=1}^m V_{\alpha_j}(\mathbf{r})$, $V_\beta(\mathbf{r}) = \sum_{j=1}^m V_{\beta_j}(\mathbf{r})$. Defining *kernel potentials* as

$$\omega_{\alpha_j} = V_{\alpha_j} - A_j u^{2\alpha}(\mathbf{r}),$$

$$\omega_{\beta_j} = V_{\beta_j} - A_j u^{2\beta}(\mathbf{r}), \tag{3.29}$$

we can rewrite equation 3.28 in terms of the kernel potentials to obtain the following Helmholtz equations

$$\begin{aligned} -\nabla^2 \omega_{\alpha_j}(\mathbf{r}) + B_j \omega_{\alpha_j}(\mathbf{r}) + A_j B_j u^{2\alpha}(\mathbf{r}) = 0 \qquad j = 1, ..., m, \\ -\nabla^2 \omega_{\beta_j}(\mathbf{r}) + B_j \omega_{\beta_j}(\mathbf{r}) + A_j B_j u^{2\beta}(\mathbf{r}) = 0 \qquad j = 1, ..., m. \end{aligned} \tag{3.30}$$

Expressing these Helmholtz equations in a variational form, we reformulate the nonlocal kernel energies in equation 3.1 as the following saddle-point problem:

$$\begin{aligned} T_K(u) = \inf_{\omega_{\alpha_j}} \sup_{\omega_{\beta_j}} \sum_{j=1}^m \Bigg\{ \int \Bigg[\frac{1}{A_j B_j} \nabla \omega_{\alpha_j}(\mathbf{r}) . \nabla \omega_{\beta_j}(\mathbf{r}) + \frac{1}{A_j} \omega_{\alpha_j}(\mathbf{r}) \omega_{\beta_j}(\mathbf{r}) \\ + \omega_{\alpha_j}(r) u^{2\beta}(\mathbf{r}) + \omega_{\beta_j}(\mathbf{r}) u^{2\alpha}(\mathbf{r}) + A_j u^{2(\alpha+\beta)} \Bigg] \mathrm{d}\mathbf{r} \Bigg\} \end{aligned}$$

The functional derivatives of the variational form derived above should be consistent with the Helmholtz equations as well as the Euler-Lagrange with respect to u. It should also reduce to the kinetic energy evaluated in $T_K(u)$. In order to verify this, we first take the functional derivatives with respect to the *kernel potentials*, w_{β_j}. As shown below, the

functional derivative with respect to w_{β_j} gives 3.30 in w_{α_j} and vice versa.

$$\frac{\delta T_K\left(u\right)}{\delta \omega_{\beta_j}} = \frac{1}{A_j}\omega_{\alpha_j}\left(\mathbf{r}\right) + u^{2\alpha}\left(\mathbf{r}\right) - \nabla.\left[\frac{1}{A_j B_j}\nabla\omega_{\alpha_j}\left(\mathbf{r}\right)\right] = 0. \tag{3.31}$$

Taking functional derivative with respect to u,

$$\begin{aligned}
\frac{\delta T_K\left(u\right)}{\delta u} &= \sum_{j=1}^{m}\left[2\beta\omega_{\alpha_j}\left(\mathbf{r}\right)u^{2\beta-1}\left(\mathbf{r}\right) + 2\alpha\omega_{\beta_j}\left(\mathbf{r}\right)u^{2\alpha-1}\left(\mathbf{r}\right) + 2A_j\left(\alpha+\beta\right)u^{2(\alpha+\beta)-1}\left(\mathbf{r}\right)\right] \\
&= \sum_{j=1}^{m}\left[2\beta u^{2\beta-1}\left(\mathbf{r}\right)\left(\omega_{\alpha_j}\left(\mathbf{r}\right) + A_j u^{2\alpha}\left(\mathbf{r}\right)\right) + 2\alpha u^{2\alpha-1}\left(\mathbf{r}\right)\left(\omega_{\beta_j}\left(\mathbf{r}\right) + A_j u^{2\beta}\left(\mathbf{r}\right)\right)\right] \\
&= \sum_{j=1}^{m}\left[2\beta u^{2\beta-1}\left(\mathbf{r}\right)V_{\alpha_j}\left(\mathbf{r}\right) + 2\alpha u^{2\alpha-1}\left(\mathbf{r}\right)V_{\beta_j}\left(\mathbf{r}\right)\right]
\end{aligned} \tag{3.32}$$

As shown above, the functional derivative of the variational form with respect to u reproduces the same expressions that would be obtained from the non-local form of kinetic energy functional, T_k. Finally, we look at the evaluation of the kinetic energy from the local variational formulation. Using integration by parts, the variational form can be reduced to:

$$\begin{aligned}
T_K\left(u\right) = &\sum_{j=1}^{m}\left\{\int_\Omega\left[-\frac{1}{A_j B_j}\nabla^2\omega_{\alpha_j}\left(\mathbf{r}\right) + \frac{1}{A_j}\omega_{\alpha_j}\left(\mathbf{r}\right) + u^{2\alpha}\right]\omega_{\beta_j}\left(\mathbf{r}\right)\,\mathrm{d}\mathbf{r}\right\} \\
&+ \sum_{j=1}^{m}\left\{\int_\Omega u^{2\beta}\left(\mathbf{r}\right)\left(A_j u^{2\alpha}\left(\mathbf{r}\right) + \omega_{\alpha_j}\left(\mathbf{r}\right)\right)\,\mathrm{d}\mathbf{r}\right\}
\end{aligned} \tag{3.33}$$

The first integral in 3.33 goes to zero due to 3.30. Hence,

$$\begin{aligned} T_K(u) &= \sum_{j=1}^{m} \left\{ \int_{\Omega} u^{2\beta}(\mathbf{r}) \left(A_j u^{2\alpha}(\mathbf{r}) + \omega_{\alpha_j}(\mathbf{r}) \right) \mathrm{d}\mathbf{r} \right\} \\ &= \sum_{j=1}^{m} \left\{ \int_{\Omega} u^{2\beta}(\mathbf{r}) V_{\alpha_j}(\mathbf{r}) \, \mathrm{d}\mathbf{r} \right\} \\ &= \int_{\Omega} u^{2\beta}(\mathbf{r}) V_{\alpha}(\mathbf{r}) \, \mathrm{d}\mathbf{r}. \end{aligned} \tag{3.34}$$

Thus, the variational formulation has been shown to be consistent with the energy and all the functional derivatives.

Having reformulated all the extended interaction terms, the ground state energy can be rewritten in a local variational in real space:

$$E_0 = \inf_{\mathbf{R}} \inf_{u} \sup_{\phi} \inf_{\omega_{\alpha_j}} \sup_{\omega_{\beta_j}} L\left(u, \phi, \omega_{\alpha_j}, \omega_{\beta_j}, \mathbf{R}\right), \tag{3.35}$$

subject to:

$$\int_{\Omega} u^2(\mathbf{r}) \, \mathrm{d}r = N, \tag{3.36}$$

where, we define the Lagrangian, $L\left(u, \phi, \omega_{\alpha_j}, \omega_{\beta_j}, \mathbf{R}\right)$, as:

$$\begin{aligned} L\left(u, \phi, \omega_{\alpha_j}, \omega_{\beta_j}, \mathbf{R}\right) = \; & C_F \int u^{10/3}(\mathbf{r}) \, \mathrm{d}\mathbf{r} + \frac{1}{2} \int |\nabla u(\mathbf{r})|^2 \, \mathrm{d}\mathbf{r} + \int \epsilon_{xc}(u(\mathbf{r})) u^2(\mathbf{r}) \, \mathrm{d}\mathbf{r} \\ & - \frac{1}{8\pi} \int |\nabla \phi(\mathbf{r})|^2 \, \mathrm{d}\mathbf{r} + \int (\rho(\mathbf{r}) + b(\mathbf{r}; \mathbf{R})) \phi(\mathbf{r}) \, \mathrm{d}\mathbf{r} \\ & + \sum_{j=1}^{m} \Bigg\{ \int \Bigg[\frac{1}{A_j B_j} \nabla \omega_{\alpha_j}(\mathbf{r}) . \nabla \omega_{\beta_j}(\mathbf{r}) + \frac{1}{A_j} \omega_{\alpha_j}(\mathbf{r}) \omega_{\beta_j}(\mathbf{r}) \\ & + \omega_{\alpha_j}(r) u^{2\beta}(\mathbf{r}) + \omega_{\beta_j}(\mathbf{r}) u^{2\alpha}(\mathbf{r}) + A_j u^{2(\alpha+\beta)} \Bigg] \mathrm{d}\mathbf{r} \Bigg\} \end{aligned} \tag{3.37}$$

3.3 Finite element approximation and numerical implementation

The local formulation presented in the previous section forms the basis for the finite element discretization. The finite element basis is composed of piecewise polynomial functions which are constructed over a discretization of the domain. The domain discretization is achieved using *elements* or triangulations based on voronoi tessellations. The most simplest of these domain discretizations result in tetrahedral elements which have been used throughout this work. Each triangulation is identified by the vertices or *nodes*. The finite element bases are constructed on these domain discretizations which are commonly referred to as *shape functions* and are associated with each node in the discretization. The shape functions are constructed to assume a value of 1 at the node to which it is associated and is zero at other nodes of the element. The triangulation size is usually denoted by the parameter h. In our case of tetrahedral elements, the parameter h represents the largest circumdiameter of all of its faces.

The electronic fields are approximated in the finite element basis as:

$$\begin{aligned} u^h(\mathbf{r}) &= \sum_i u_i N_i^h(\mathbf{r}) \\ \phi^h(\mathbf{r}) &= \sum_i \phi_i N_i^h(\mathbf{r}) \\ \omega^h(\mathbf{r}) &= \sum_i \omega_i N_i^h(\mathbf{r}) \end{aligned} \tag{3.38}$$

where, i is the index of the nodes, $N_i^h(\mathbf{r})$ is the shape function associated with the node i and u_i, ϕ_i, ω_i are the values of the fields $u^h(\mathbf{r}), \phi^h(\mathbf{r}), \omega^h(\mathbf{r})$ at the node i respectively. The convergence of the finite element discreization has been shown rigorously using Γ convergence, which is a variational notion of convergence for non-linear functionals, in

Ref. [21].

Having discretized the local real space formulation of the *orbital free* density functional theory using finite element approximation, the problem of finding the ground state has been reduced to solving an array of nodal values: u_i, ϕ_i, ω_i. This is achieved using a nested sequence inexact Newton solvers provided by KINSOL [50] and PETSc [51]. For a fixed set of atomic positions, we solve for root of electron density, u_i, and for each u_i, we solve for the electrostatic and kernel potentials, ϕ_i and ω_i respectively. A detailed analysis of various efficient solution procedures, staggered and simultaneous approach, can be found in Ref. [49].

The local variational structure facilitates the use of finite element approximation to solve the optimization problem of finding the ground state energy. The local nature of the formulation also makes it easy to use the widely available parallel architecture. This allows to solve for large degrees of freedom in a given time frame. Further sections in this chapter are based on this local formulation and the finite element framework. In particular, we will take advantage of the ability to coarse grain the triangulations to achieve million-atom electronic structure calculations.

3.4 Bulk properties

Having implemented the local variational formulation in a real-space finite element basis, we perform benchmark calculations to verify the accuracy of the approximation and compare it with the available results from plane-wave basis implementations available in the literature. As a first step, we perform bulk calculations on periodic unit cells of aluminium. We use Goodwin-Needs-Heine local pseudo potential [52]. We perform these bulk calculations for both the density independent as well as density dependent variants of the WGC

kinetic energy potentials. In the case of density dependent kinetic energy potentials, we have restricted ourselves to the first order Taylor series expansion of the kernel function. The figures 3.3 and 3.4 show the variation of the ground state energy per atom with respect to the lattice parameter. The Bulk modulus is calculated using [15]:

Figure 3.3: Bulk modulus calculation of Aluminium using density independent Wang-Govind-Carter kinetic energy functional. Variation of energy per atom for various values of the lattice parameter

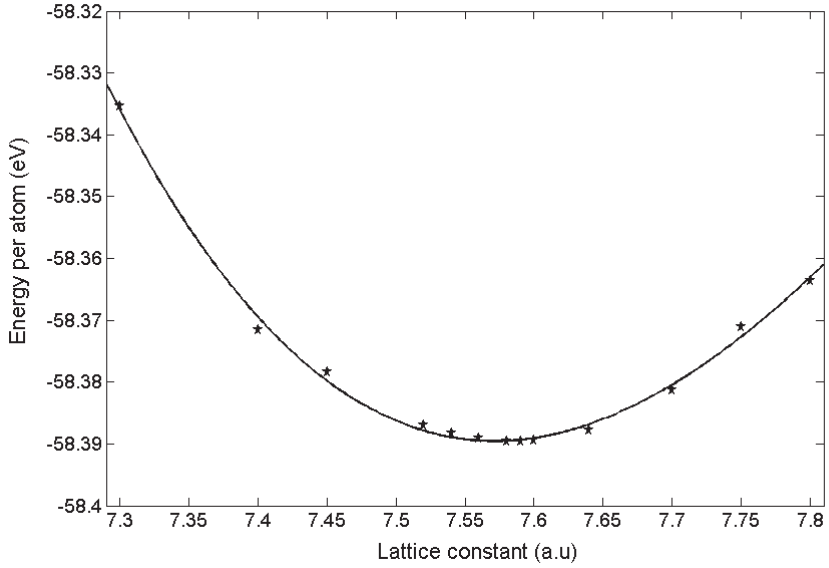

$$K = V_c \frac{\partial^2 E}{\partial V_c^2}, \tag{3.39}$$

where, V_c is the equilibrium volume of the unit cell. Table 3.2 below shows the bulk properties predicted using the real-space local variational implementation. The computed bulk properties are in good agreement with those computed from plane-wave basis.

Figure 3.4: Bulk modulus calculation of Aluminium using density dependent Wang-Govind-Carter kinetic energy functional. Variation of energy per atom for various values of the lattice parameter

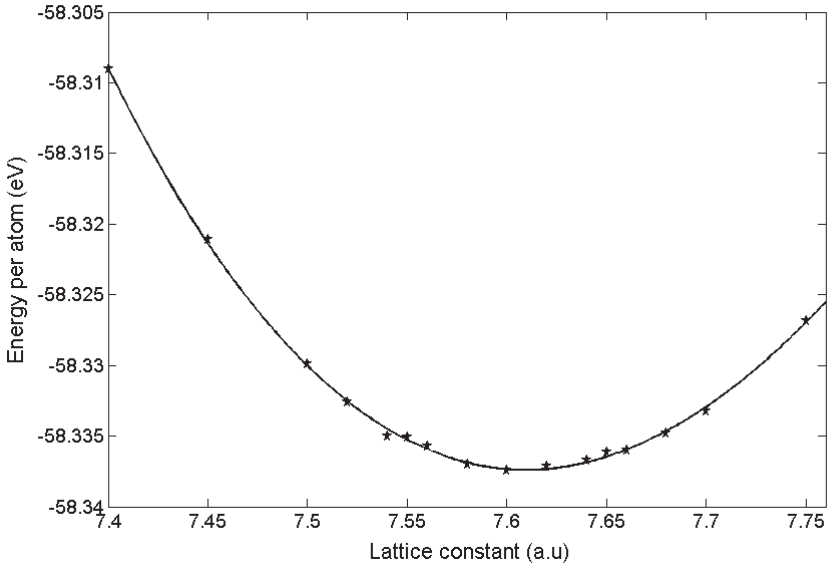

Table 3.2: Bulk Properties of Aluminium

Properties	KSDFT (Refs. [29, 2])	OF-FS (DI) [1]	OF-RS (DI)	OF-FS (DD) [29]	OF-RS (DD)
Bulk modulus (GPa)	68.5	71.9	72	72	71.92
Energy per atom (eV)	-58.33	-58.33	-58.38	-58.33	-58.33
Lattice constant (a.u)	7.62	7.59	7.58	7.61	7.6

3.5 Quasi Continuum Orbital free density functional theory

The *orbital-free* density functional theory implementation is computationally less expensive compared to the *Kohn-Sham* implementation as explicit computations of the single-electron wave-functions are avoided. Nevertheless, OFDFT simulations are expensive enough to limit the system size to a few thousand atoms. While such system sizes are sufficient to simulate bulk properties of even complex alloys like Al_xMg_y, they may not be large enough to simulate defects. In fact, such cell-size restrictions can lead to prediction

of spurious physics. A complete understanding of defects required not only an accurate description of the electronic structure close to the defect-core but also capturing the long ranged elastic and electro-static fields away from the defect-core. Hence, there is a necessity to perform electronic structure calculations at macroscopic scales.

In this section, we present the coarse graining technique, Quasi-Continuum *orbital free* density functional theory (QCOFDFT). QCOFDFT is a seamless technique that enables us to perform multi-million atom simulations at the computational cost comparable to a few thousand atom simulation. The technique uses *orbital free* as the sole input physics thereby achieving electronic structure calculation at macroscopic scales. The QC reduction was previously developed in the context of the local kinetic energy functionals [21]. In this work, the QC reduction is extended to the non-local kinetic energy functionals based on the local variational formulation developed in the previous section. Here, we present the key ideas in the QC reduction and predict the energetics of mono and di-vacancies in aluminium.

Simulation-cell size restrictions have been addressed before in other atomistic calculations, in particular, inter-atomic potential based methods, using different schemes leading to various multi-scale methods [53, 54, 55]. The core idea in such multi-scale schemes is an effort to bridge atomistics and continuum theories. One of the most popular and comprehensively studied multi-scale methodology is the Quasi-Continuum reduction. The Quasi-continuum reduction was initially proposed in the context of inter-atomic potentials as a seamless scheme that bridged atomistic and continuum length scales [53]. Defects produce atomic scale perturbations to the positions of nuclei close to the defect-core. But, away from the defect-core, the displacements vary only on a macroscopic length scale. Introducing the concept of representative atoms (*repatoms*), the atomic positions are coarse-grained such that all the nuclei are represented close to the defect-core, while few chosen

repatoms are enough to capture the displacement fields away from the defect-core. The nuclear positions away from the defect-core are kinematically constrained to the *repatoms* using the shape functions of a finite-element triangulation of the repatoms. Thus, the degrees of freedom required to perform multi-million atom simulations are greatly reduced to a few hundred to a few thousands of *repatoms* (depending on the complexity of the defect). The forces and energy terms are approximated using cluster summation rules to make all calculations to be commensurate with the number of representative atoms. The number of representative atoms can be increased progressively to obtain convergence. A theoretical estimate of the convergence rates has been derived in [56] and a thorough discussion of various schemes of the Quasi-Continuum reductions can be found in [57].

Efforts have also been directed towards overcoming cell-size restrictions in electronic structure calculations. One such multi-scale seamless scheme is the Quasi-Continuum reduction of the orbital-free density functional theory proposed by Gavini et. al [21]. The Quasi Continuum reduction is based on

- a real-space local formulation of the orbital-free density functional theory
- finite element discretization
- an adaptive coarse graining of the mesh

In the presence of defects, both displacements of nuclei and electronic fields vary rapidly near the defect core. However, away from the defect core the displacement fields are smooth and vary only on a macroscopic length scale, and in these regions the electronic fields are locally periodic i.e., electronic fields exhibit the periodicity of the underlying lattice which changes only on a macroscopic length-scale. This structure is exploited to develop the QC reduction in the formulation.

To this end, three unstructured triangulations of the domain are introduced: T_{h_1}, T_{h_2} and T_{h_3} as shown in Figure 3.5.

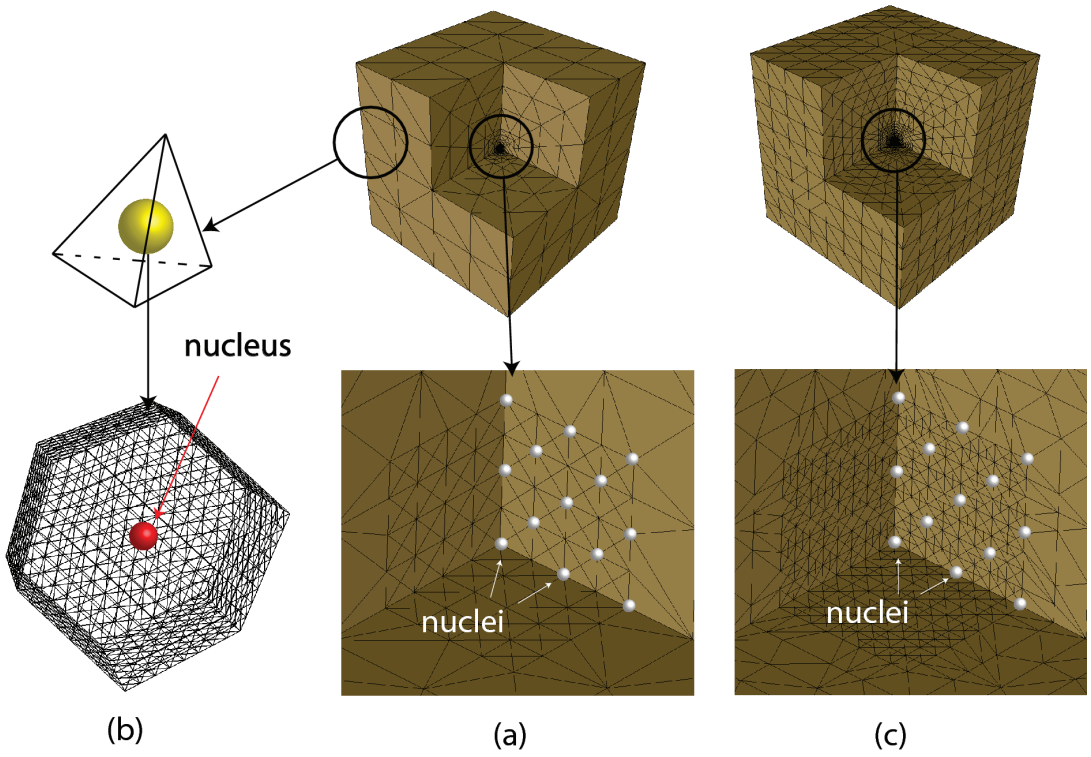

Figure 3.5: (a) T_{h_1}: Atomic mesh used to interpolate positions of nuclei away from the fully resolved defect core. (b) T_{h_2}: Auxiliary mesh used to sample the predictor fields within a unit cell. (c) T_{h_3}: Electronic mesh used to represent the corrector fields. It has subatomic resolution in the defect core, and coarsens away from the defect core.

First, the displacement fields are resolved using a finite-element triangulation of selected nuclei called representative nuclei (repatoms), T_{h_1}, and interpolating the positions of all nuclei using the positions of these representative nuclei. The representative nuclei are chosen such that all nuclei are resolved near the defect core whereas away from defect core, where the displacement fields are smooth, the resolution becomes coarser and a

small fraction of the nuclei is used to determine the positions of the rest. The coarse graining algorithm adopted here is akin to that used in the case of interatomic potentials based Quasi-continuum method.

To extend the coarse-graining techniques to the electronic fields, they are decomposed into predictor fields and corrector fields.

$$\begin{aligned} u^h =& u_0^h + u_c^h, \\ \phi^h =& \phi_0^h + \phi_c^h \text{ and} \\ \omega^h =& \omega_0^h + \omega_c^h. \end{aligned} \tag{3.40}$$

The predictor fields (u_0^h, ϕ_0^h and ω_0^h) are represented on a finite-element triangulation, T_{h_2}, of unit cells contained within each element of the atomic mesh, and are computed using a periodic calculation with the deformation of the underlying lattice. In the above equation 3.40, for the sake of simplicity, we use "ω" to denote the set of all kernel potentials. The predictor fields accurately capture the locally periodic electronic structure away from the defect core but provide a very inaccurate representation of the electronic structure close to the defect core. The corrector fields, which correct for these inaccuracies, are thus represented on a finite-element triangulation, T_{h_3}, that is subatomic close to the defect core and coarse grains away to become superatomic. As a matter of convenience, the electronic mesh is chosen to be a uniform subdivision of the atomic mesh, thus increasing the resolution in the corrector fields with increasing resolution in the displacement field.

Using the decomposition from equation 3.40, the independent variables of the formulation reduce to the coarse-grained variables comprising of the representative nuclei and corrector electronic fields. Hence, the exercise of finding the ground state energy is now

reduced to a constrained optimization problem over the corrector fields:

$$\inf_{u_c^h} \sup_{\phi_c^h} \inf_{\omega_c^h} L\left(u_0^h + u_c^h, \phi_0^h + \phi_c^h, \omega_0^h + \omega_c^h\right) \tag{3.41}$$

The calculated predictor fields are not necessarily continuous across T_{h_1} elements. To maintain the continuity of the predictor fields, u_0^h, ϕ_0^h and ω_0^h, we perform a $L^2 \rightarrow H^1$ map. In practice, this is achieved by averaging the value at any nodal location from all the contributions from T_{h_1} elements sharing the node.

The predictor fields are computed on the uniformly sub-divided T_{h_2} mesh. Thus, the computational complexity of the system is still commensurate with the T_{h_2} triangulation. But, using the cluster summation rules in QC [56], the following integration rules were introduced [21] to reduce all the computations to the complexity of T_{h_3}:

$$\int_e g\left(\mathbf{r}\right)\, \mathrm{d}\mathbf{r} \approx |e| \left\langle g \right\rangle_{D_e} \tag{3.42}$$

where, $|e|$ is the volume of an element $e \in T_{h_3}$, D_e is the unit cell of an atom if such cell is contained in e or e otherwise and $\left\langle g \right\rangle_{D_e}$ is the average of g over D_e. Hence any integral over the domain can be evaluated as:

$$\int_\Omega g\left(\mathbf{r}\right)\, \mathrm{d}\mathbf{r} = \sum_{e \in T_{h_3}} \int_e g\left(\mathbf{r}\right)\, \mathrm{d}\mathbf{r} \approx \sum_{e \in T_{h_3}} |e| \left\langle g \right\rangle_{D_e} \tag{3.43}$$

Having defined the triangulations used in the Quasi-continuum reduction and the reformulation of the ground state energy in terms of the corrector fields, we now proceed to computing the forces and energies across the triangulations.

The energy functional in orbital free DFT, based on the functional form of the inte-

grands, can be written as

$$L\left(u^h,\phi^h,\omega^h,\mathbf{R}\right)=\int_\Omega g\left(u^h,\nabla u^h,\omega^h,\nabla\omega^h\right)d\Omega+\int_\Omega\left(\left(u^h\right)^2+\sum_i Z_i b_i\right)\phi^h d\Omega \\ -\frac{1}{8\pi}\int_\Omega\left|\nabla\phi^h\right|^2 d\Omega \tag{3.44}$$

where b_i represents the regularized nuclear charge with charge Z_i on the i^{th} node. The nodal forces corresponding the corrector fields on the k^{th} node is given as

$$f_u^k\left(u^h,\phi^h,\omega^h,\mathbf{R}\right)=\frac{\partial L\left(u^h,\phi^h,\omega^h,\mathbf{R}\right)}{\partial u_{c_k}^h}$$

$$f_\phi^k\left(u^h,\phi^h,\omega^h,\mathbf{R}\right)=\frac{\partial L\left(u^h,\phi^h,\omega^h,\mathbf{R}\right)}{\partial \phi_{c_k}^h}$$

$$f_\omega^k\left(u^h,\phi^h,\omega^h,\mathbf{R}\right)=\frac{\partial L\left(u^h,\phi^h,\omega^h,\mathbf{R}\right)}{\partial \omega_{c_k}^h} \tag{3.45}$$

We consider the generalized force with respect to ϕ_{c_k}, (f_ϕ^k), to detail the exact computational steps involved, and is given by:

$$f_\phi^k\left(u^h,\phi^h,\omega^h,\mathbf{R}\right)=\int_\Omega\left(\left(u^h\right)^2+\sum_i Z_i b_i\right)N_k^{h_3}d\Omega-\frac{1}{8\pi}\int_\Omega\nabla\phi^h.\nabla N_k^{h_2}d\Omega \tag{3.46}$$

where $N_k^{h_3}$ is the shape function associated with node k of T_{h_3} triangulation. Though the corrector fields are defined on the nodes of T_{h_3}, the forces need to be computed using fields defined on the uniform mesh T_{h_2}. By construction, T_{h_2} is a sub-grid of T_{h_3}. As the shape functions are linear,

$$N_k^{h_3}(r)=\sum_{a\in T_{h_2}}N_k^{h_3}(a)\,N_a^{h_2}(r) \tag{3.47}$$

where a is the node in T_{h_2} and $N_a^{h_2}$ is the shape function associated with node a of triangu-

lation T_{h_2}. Thus the force with respect to ϕ is rewritten as

$$f_{\phi}^{k}\left(u^{h},\phi^{h},\omega^{h},\mathbf{R}\right) = \sum_{a\in T_{h_2}} N_{k}^{h_3}(a)\,\{\int_{\Omega}\left(\left(u^{h}\right)^{2}+\sum_{i} Z_i b_i\right) N_{a}^{h_2} d\Omega - \frac{1}{8\pi}\int_{\Omega}\nabla\phi^{h}.\nabla N_{a}^{h_2} d\Omega\}$$

$$= \sum_{a\in T_{h_2}} N_{k}^{h_3}(a)\, f_{\phi}^{0^a}\left(u^{h},\phi^{h},\omega^{h},\mathbf{R}\right) \tag{3.48}$$

where $f_{\phi}^{0^a}\left(u^{h},\phi^{h},\omega^{h},\mathbf{R}\right)$ is the force corresponding to ϕ on the node $a \in T_{h_2}$. The other generalized forces are similarly evaluated. Given that the T_{h_3} triangulation is designed to coarse grain, the generalized force expression, on using the cluster expansion rules, is obtained as

$$f_{\phi}^{k}\left(u^{h},\phi^{h},\omega^{h},\mathbf{R}\right) = \sum_{e\in T_{h_3}} C_e\{\sum_{a\in D_e}{}' f_{\phi}^{0^a}\left(u^{h},\phi^{h},\omega^{h},\mathbf{R}\right) N_{k}^{h_3}(a)\} \tag{3.49}$$

where, C_e is a multiplicative scalar whose value is 1 if $D_e = e$, $\frac{|e|}{D_e}$ otherwise. Essentially, it represents the number of units cells, if any, contained in the coarse grained element $e \in T_{h_3}$. The $'$ on the summation is to avoid double counting. Similar expressions can be derived for f_{u}^{k} and f_{ω}^{k}.

Previously, we had presented the implementation steps to obtain the ground state energy for a given configuration of the nuclei. In other words, the nuclei are fixed at a given set of coordinates in $\mathbb{R}^3$ and the electronic fields are relaxed to obtain the ground state energy. But, the final relaxed position would involve optimization of the ground state energy with respect to position of the nuclei: $\mathbf{R}_1, \mathbf{R}_2, \mathbf{R}_3....\mathbf{R}_M$. To this end, the configurational forces are derived in the spirit of the Eshelby's formulation for force on a defect and we refer to the work done in Ref.([58, 57]).

3.6 Monovacancy

Having formulated a coarse graining technique based on the local variational formulation, we apply our implementation on the most simplest of defects, a monovacancy. To establish the efficacy of the proposed Quasi-continuum reduction, we compute the monovacancy formation energy in aluminium using a cell-size containing 16 384 nominal number of atoms with different levels of coarse graining that is controlled by the number of representative nuclei. The results of this study for both density dependent and density independent models in OFDFT are shown in Figure 3.6. As is evident from the plot, less that 200 representative

Figure 3.6: Convergence of coarse graining approximation

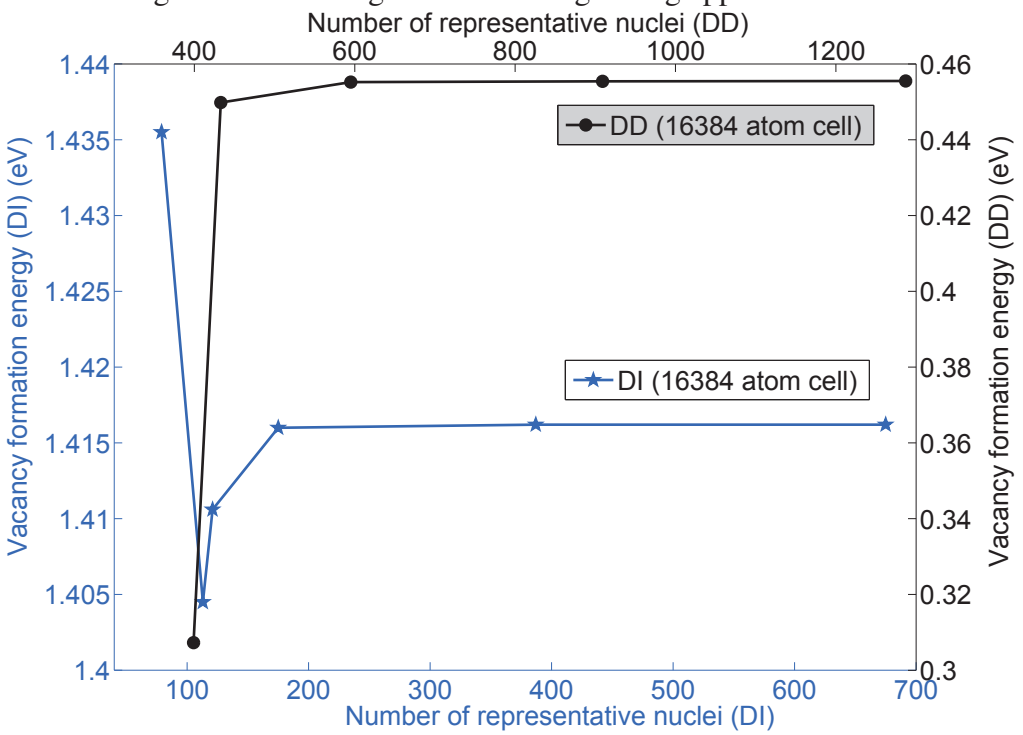

nuclei in the density independent and 600 nuclei in the case of density dependent kernels are sufficient to obtain convergence with respect to coarse graining. This significant reduction in the computational cost afforded by the proposed QC reduction makes possible an electronic structure study of defects without cell-size restrictions, where defects can be

studied under naturally occurring concentrations in materials.

Having established the convergence with respect to coarse graining, we now proceed to investigate the cell-size effect on the formation energy of a monovacancy. To this end, using both DI and WGC-DD OFDFT models, we computed the monovacancy formation energy in aluminium for varying cell-sizes from 32 atoms to a million atoms, and these results are shown in Figure 3.9. In the case of WGC-DD model, the kernel energy is expanded about the average bulk electron-density before introducing the vacancy. Homogeneous Dirichlet boundary conditions are imposed on the corrector electronic fields as well as the displacement fields in all computations, which imply that the perturbations in electronic and displacement fields in the presence of these defects vanish on the boundaries of the sample. The numerical parameters including mesh size and coarse-graining rates are chosen such that the numerical error in computed formation energies is less that 0.01 eV. Figure 3.7 shows the electron density contours of a monovacancy. The $n-$ vacancy formation energy

Figure 3.7: Electron density contours of monovacancy in Aluminium

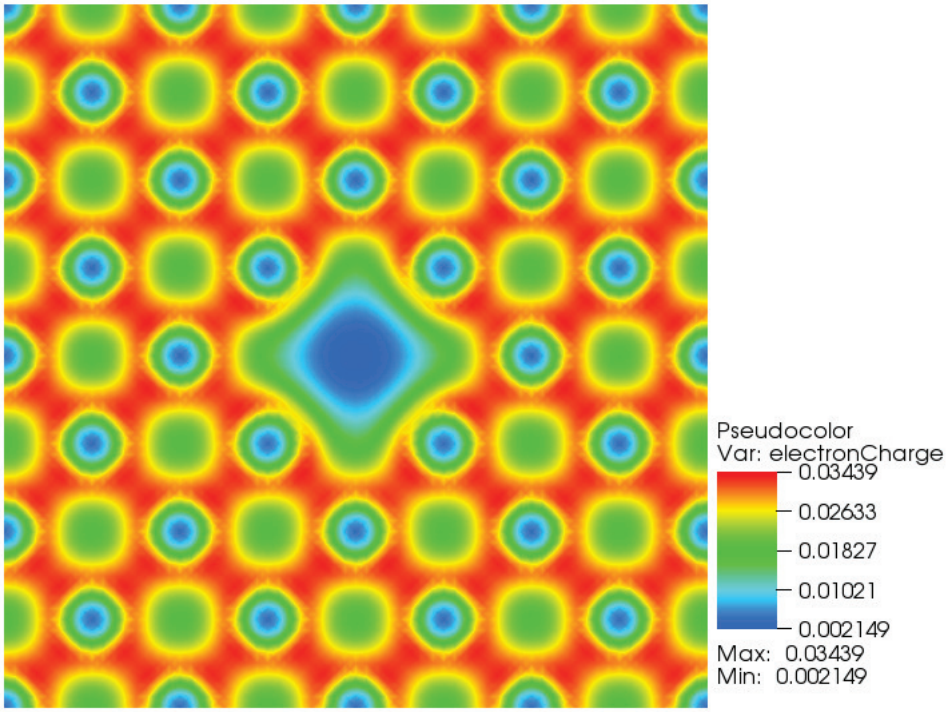

is computed using the following expression:

$$E_{nv}^{f} = E\left(N-n, n, \frac{N-n}{N}V\right) - \frac{N-n}{N}E\left(N, 0, V\right), \tag{3.50}$$

where, E_{nv}^{f} is the formation energy of a n vacancy system, $E\left(N-n, n, \frac{N-n}{N}V\right)$ is the energy of an $N-n$ atom system containing n vacancies occupying a volume of $\frac{N-n}{N}V$. The formation energy is computed by comparing the energy of an $N-n$ atom system with $n-$ vacancies occupying the same volume as that of an perfect crystal of $N-n$ atoms.

The monovacancy formation energy computed using a 32 atoms computational cell is 1.33 eV for DI model and 0.54 eV for WGC-DD model, and these results are in very good agreement with those reported in the literature. DI kernels are known to be inaccurate in predicting the monovacancy formation energy in aluminium, which is estimated to be 0.51 eV using KSDFT on a 32 atoms computational cell [59] and 0.66 eV from experiments [60]. However, in this study, we focus our attention on the cell-size effects. As seen from Figure 3.9, there is a remarkable cell-size dependence in the computed formation energy of a vacancy. These results indicate that cell-sizes on the order of $10^3 - 10^4$ atoms are required to obtain convergence with respect to cell-size even in simple defects such as vacancies. We attribute these cell-size effects to the long-ranged nature of the displacement fields, which is well known from studies on defects using continuum elasticity, as well as the slower than expected decay in the perturbations of electronic fields arising in the presence of defects. Our numerical calculations suggest that nonlinear effects dominate up to a distance of $2-3$ lattice units away from the vacancy-core, only beyond which the expected exponential decay is observed. Moreover, the perturbations in the electronic fields are strong enough to be felt up to a distance of 5 lattice units from the vacancy.

We note that a formal justification using perturbation method and multi-scale analysis

was provided in Ref.([3]). In this work, a perturbation that simulated a defect like vacancy is introduced. Following a perturbation analysis, the homogenized equations that determine the behavior of the corrector fields are derived. These equations are then analyzed to show that far away from the defect core, the corrector fields do not exhibit atomic scale oscillations, thus, also providing a formal justification for the quasi-continuum reduction. The corrector fields that were obtained for the electrostatic potential were compared with the theoretical estimates from this work and the behavior of the corrector field is plotted below.

Figure 3.8: The decay of the corrector to the electrostatic potential ϕ_c^h is compared with the theoretical estimates from the Quasi continuum analysis [3]

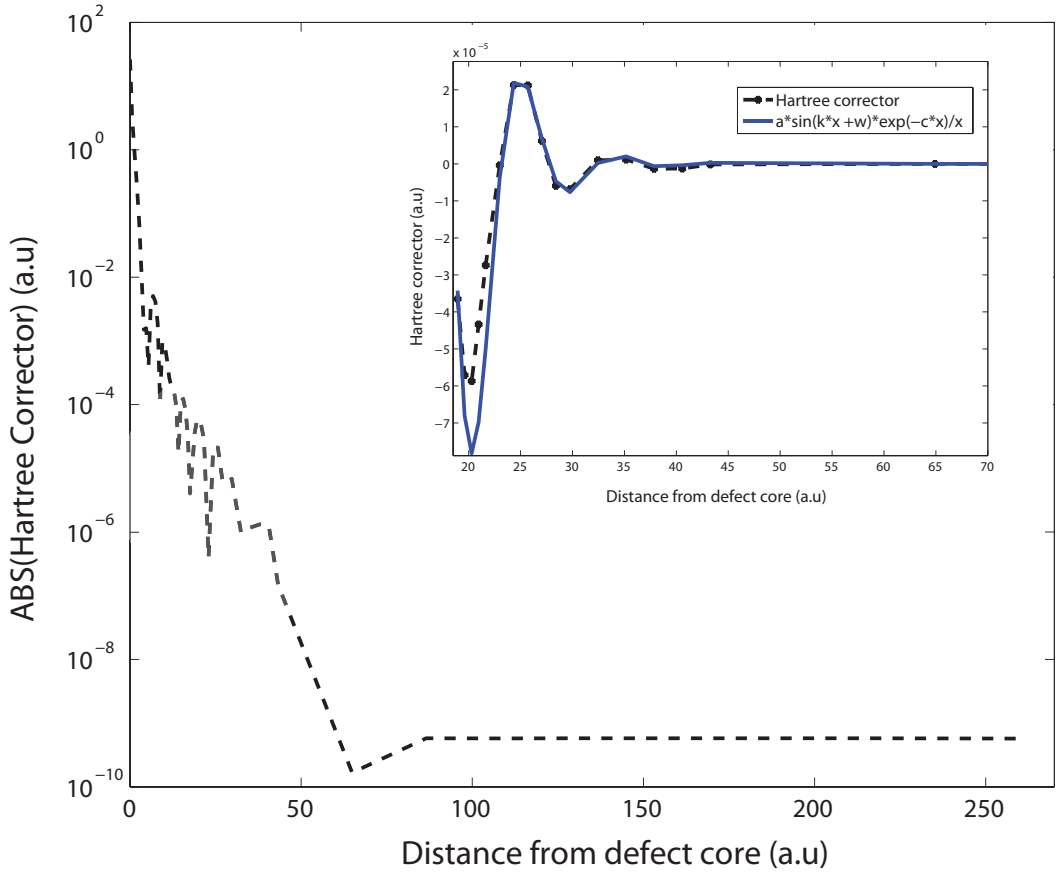

The difference in monovacancy formation energies computed using a commonly used

32 atoms cell-size and the more realistic dilute limit corresponding to a million-atoms cell-size is on the order of 0.1 eV, which may appear insignificant at first. However, we note that the interaction energies between vacancies are on the order of 0.1 eV and are significantly influenced by these cell-size effects.

Figure 3.9: Cell-size study of monovacancy in Aluminium

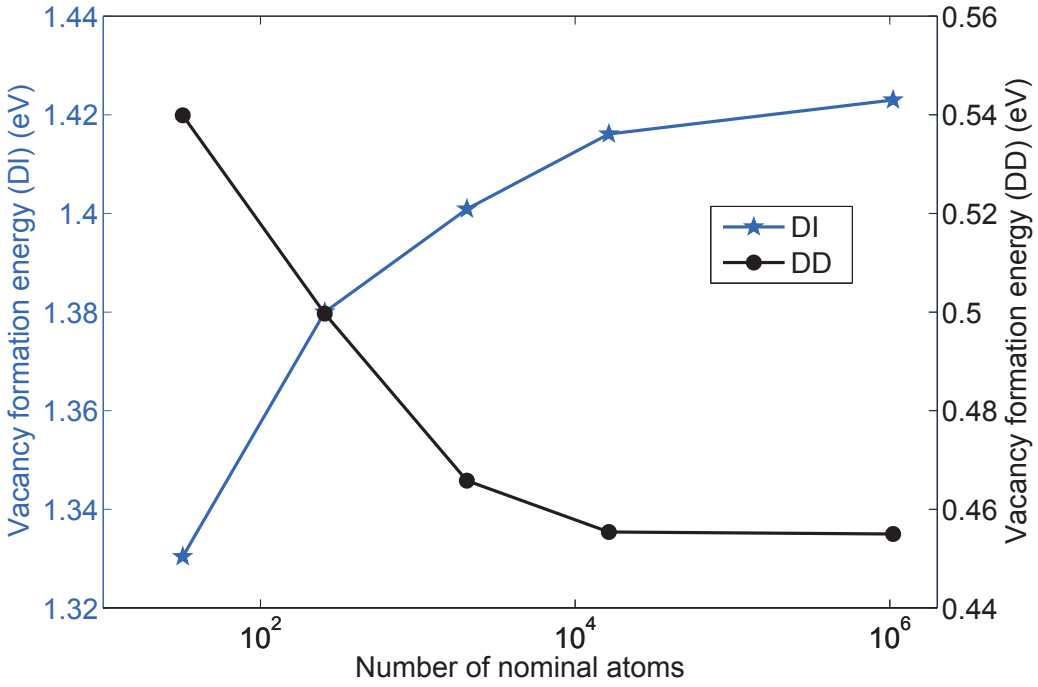

3.7 Di-vacancy binding energy

Having demonstrated the cell-size effect in the case of monovacancy in aluminium in the last section, in this section, we will show the significance of performing large cell-size simulations using di-vacancy studies. To this end, we consider both $\langle 110 \rangle$ and $\langle 100 \rangle$ di-vacancies in aluminium. Cell-size studies similar to monovacancy are performed for both the di-vacancies using WGC-DI and WGC-DD kinetic energy functionals. Figures 3.10 and 3.11 show the electron density contours of the $\langle 110 \rangle$ and $\langle 100 \rangle$ di-vacancies in alu-

minium.

Figure 3.10: Electron density contours of $\langle 110 \rangle$ di-vacancy in Aluminium

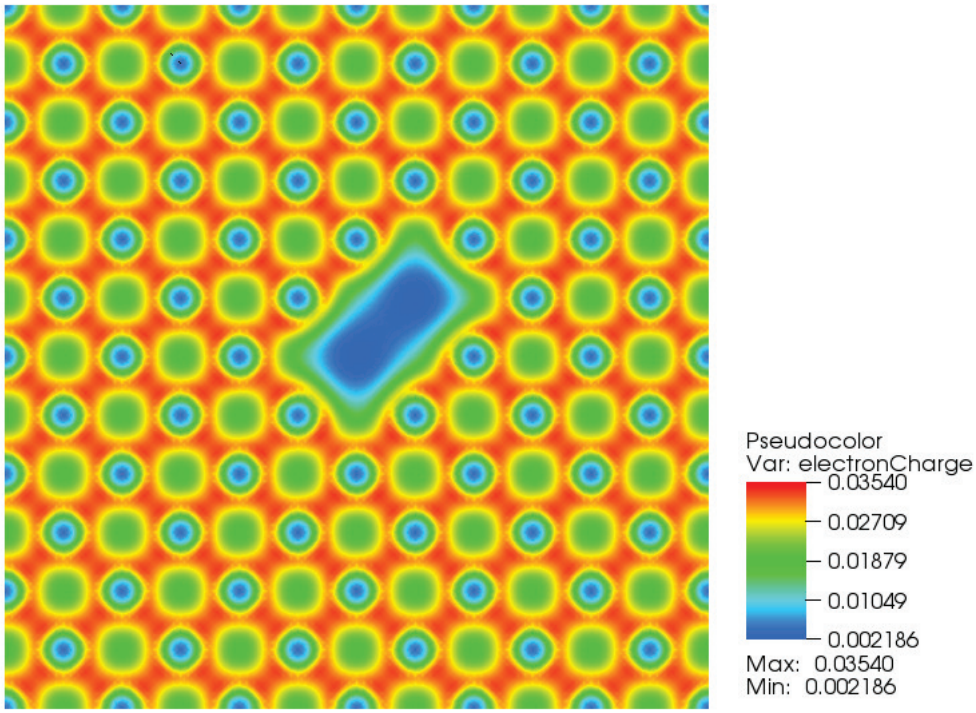

Figure 3.11: Electron density contours of $\langle 100 \rangle$ di-vacancy in Aluminium

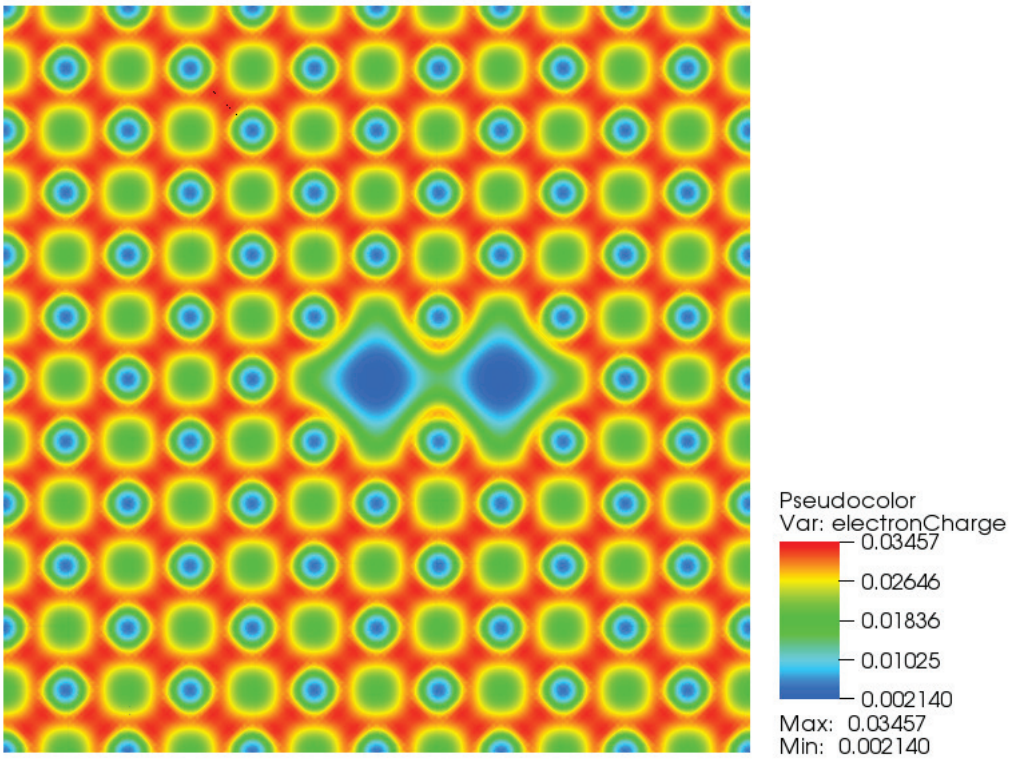

Using different cell-sizes, we predict the binding energies for both the di-vacancies. The binding energy for a $n-$ vacancy cluster is calculated using the formula:

$$E_{nv}^{bind} = nE_v^f - E_{nv}^f \tag{3.51}$$

where, E_{nv}^f is the formation energy of a $n-$vacancy system (equation 3.50) and E_v^f is the formation energy of monovacancy.

Figure 3.12 shows the cell-size effect on the binding energies of di-vacancies in aluminium. Monovacancy studies have shown that the density independent kinetic energy functionals are inaccurate and the WGC-DD kinetic energy functionals are more dependendable. Here, for the sake of completeness, we have computed the binding energies for both the density independent as well as density dependent WGC kinetic energy functionals. But, we will restrict our analysis to the results obtained using WGC-DD. The results

Figure 3.12: Cell-size study of di-vacancy binding energies in aluminium

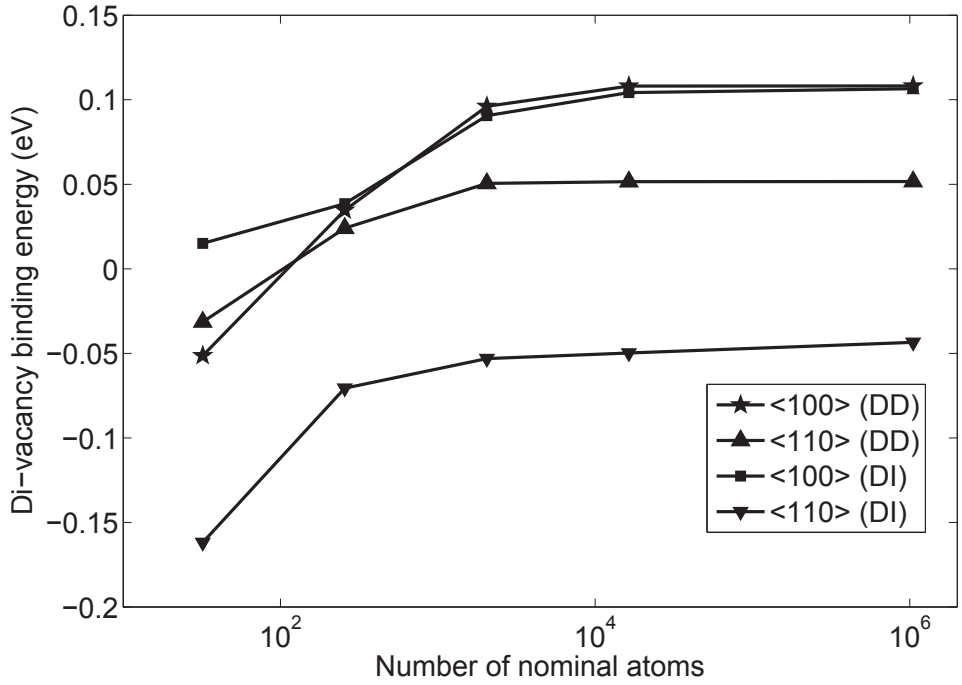

show that, when the defects are simulated in a cell-size of 32 atoms, the di-vacancy binding energies are negative, indicating repulsion between the vacancies. It would be energetically favourable for the defects to stay as isolated monovacancies rather than form a stable di-vacancy. But, as the cell-sizes are increased, we see that the binding energy energy becomes more positive predicting attraction in keeping with experimental investigations. In the present study, convergence in the binding energy is obtained around 10^3 atoms.

3.8 Summary

In this chapter, we have discussed the limitations of using plane-wave basis in implementation of *orbital free* density functional theory. To address these limitations, we have proposed a real-space local variational formulation. To this end, we reformulated the non-local kinetic energy functionals to a local variational saddle point problem. Using this formulation, we have implemented a finite element based approach that can handle arbitrary boundary conditions. Bulk properties of aluminium were calculated and shown to be consistent with the plane-wave implementations. The limitations on the cell-size due to computational cost is addressed using the Quasi-continuum reduction of the *orbital free* density functional theory. In this work, the Quasi-continuum reduction was extended to the non-local kinetic energy functionals and studies were conducted on million-atom simulation cells. Mono-vacancy and di-vacancy studies clearly demonstrated that much larger cell-sizes ($\sim 10^4$ atoms)are required to make contact with experimental observations.

Having performed benchmark defect calculations using the Quasi Continuum reduction, we proceed towards much more complex problems of interest in the next chapters. To this end, we study the dislocation-core of a single edge dislocation in aluminium and predict its energetics. We also explore the effect of deformation on the energetics of the dislocation-core.

CHAPTER 4

Electronic structure calculations of an edge dislocation

In chapter 3, we presented ideas based on a real space local variational formulation that can achieve million atom simulations with arbitrary boundary conditions. Using the Quasi Continuum reduction, we showed the need to study defects in their realistic concentrations to make contact with experiments. Having established the efficacy of the method in simulating simple defects, we proceed towards investigating more complex defects and their energetics. To this end, we conduct electronic structure calculations of an isolated edge dislocation in aluminium.

Dislocations and their interactions with other defects—solute atoms, precipitates, grain boundaries, surfaces and interfaces—significantly influence the mechanical properties in crystalline materials [5, 61, 62, 63, 64, 65]. For instance, the kinetic barriers for dislocation motion—dislocation glide and climb—and their dependence on crystallographic planes and directions govern ductility and creep in metals [66, 67, 68, 69]. Interaction of dislocations with vacancies, solute atoms and precipitates results in solid-solution strengthening/softening, precipitate hardening and aging in metals [70, 71, 63, 72, 65]. Further, dislocation interactions with grain boundaries and surfaces are responsible for the observed strengthening mechanisms like the Hall-Petch effect [73], and enhanced yield strength in surface dominated nanostructures [62, 74].

The behavior of dislocations (nucleation, kinetics, evolution) in crystalline materials is governed by physics on multiple length-scales. In particular, a dislocation produces elastic fields that are long-ranged, and through these elastic fields interacts with other defects and external loads at macroscopic scales. On the other hand, the quantum-mechanical and atomistic-scale interactions play an important role in governing the nucleation and kinetics of these defects. While the atomistic-scale interactions can significantly influence the behavior of dislocations, these are localized to a region around the dislocation line referred to as the dislocation-core. Continuum theories based on elastic formulations have been widely used to study deformation and failure mechanisms mediated through dislocations [75, 76, 77, 78, 79], where the energetics of dislocations are solely determined by the elastic energy and the core-energy is often assumed to be an inconsequential constant. In order to overcome the inability of continuum theories to describe the dislocation-core, atomistic calculations based on empirical interatomic potentials have been employed and have provided many useful insights [8, 9, 10, 11, 12, 13]. However, the interatomic potentials, whose parameters are often fit to bulk properties and some defect properties, may not accurately describe the dislocation-core which is governed by the electronic-structure [80, 81, 82].

Efforts employing plane-wave density functional theory (DFT) calculations have focused on predicting the atomistic structure of dislocation-cores and dislocation-solute interactions in crystalline materials with different symmetries [81, 83, 82, 84, 72]. The displacement fields produced by isolated dislocations are not compatible with periodic boundary conditions, and thus, these calculations have either been restricted to either an artificial dipole and quadrapole configurations of dislocations or free-surfaces have been introduced to contain isolated dislocations. While these studies have provided useful insights into the dislocation core-structure, a direct quantification of the dislocation core-energy and its role in governing dislocation behavior, which is significant as demonstrated in this work, was

beyond reach and has been elusive thus far.

In this chapter, we will first present the ideas used in Continuum theories to predict the far-field elastic fields. We also present ideas that were used in other DFT studies performed so far, to study the dislocation-core and their limitations in predicting the energetics of an isolated dislocation in equilibrium with the bulk. In addressing these limitations, we present our work wherein, we study an isolated edge dislocation in equilibrium with the bulk of the material. We predict the size of an isolated edge dislocation-core based on the contribution of the electronic perturbations from the defect-core to the energetics of the dislocation. Then, we predict the separation distance between the Shockley partials.

The dislocation-core is often considered inconsequential while studying the interaction of dislocations [85]. Studies performed on the effect of deformation on vacancies show that the defect core-energy is not an inconsequential constant and depends significantly on macroscopic volumetric strains [86]. Motivated by these results, we studied the effect of volumetric deformation on the dislocation core-energy and discuss how they can play an important role in dislocation interactions.

4.1 Continuum modeling of dislocations

Crystalline materials are made of periodic array of atoms. In the case of a perfect crystal, the magnitude of the shear stress, referred as *flow stress*, required to produce plastic deformation has been computed using various models. One of the most earliest models of the flow stress based on the crystalline nature of the material was proposed by Frenkel [5, 87]. Assuming periodicity of the energy profile,

$$\sigma = \sigma_{theor} sin \frac{2\pi x}{b},$$

where, b is the periodicity of the energy, σ_{theor} is the estimate of the flow stress from this model and σ is the externally applied load. If x is the displacement caused due to the external load, then using Hooke's law,

$$\sigma = \mu \frac{x}{d}$$

where, μ is the shear modulus and d is the interplanar distance in the crystal. In this case, small strain limit approximation ($sin(2\pi x/b \sim 2\pi x/b)$ has been applied. From the above equations, one can estimate the approximate value of the flow stress to be

$$\sigma_{theor} = \frac{\mu b}{2\pi d} \sim \frac{\mu}{5}$$

But, experimental calculations of the flow stress showed that the resolved shear stress required to initiate plastic flow to be of the order of $10^{-3} - 10^{-5}\mu$. Metals were found to plastically deform at much smaller stresses than the theoretical estimates derived from a perfect arrangement of atoms in the crystalline structure. To explain this discrepancy, the presence of dislocations were postulated and the movement of these defects at very low stress levels leads to plastic deformation [88, 89]. X-ray diffraction techniques also provided extensive experimental evidence of the presence of dislocations due to the selective diffraction around dislocation core arising from the strain fields [90].

In order to understand the structure of a dislocation, consider a block of material as shown in figure 4.1. Cut this material along a plane till it reaches the middle of the material block. Deform the left and right section of the cut material such that a half-plane of material of thickness $|\mathbf{b}|$ can be inserted through this cut. Such an insertion causes the material close to the edge of the cut to deform extensively while away from the cut, the material is much less strained. The edge of the inserted half-plane, referred to as the dislocation line, is

given by the unit tangent vector ξ. The above description of a simple edge dislocation is called the *Volterra* dislocation. Description of the screw dislocation is on similar lines with deformation along the dislocation line. Most of the mathematical descriptions of dislocations, especially Continuum theories, are based on the *Volterra* dislocation.

Figure 4.1: A volterra edge dislocation. (a) shows the cut along the X axis of an undeformed material (b) shows the deformation introduced in the material block to create a displacement equal to the burger's vector $\mathbf{b}$

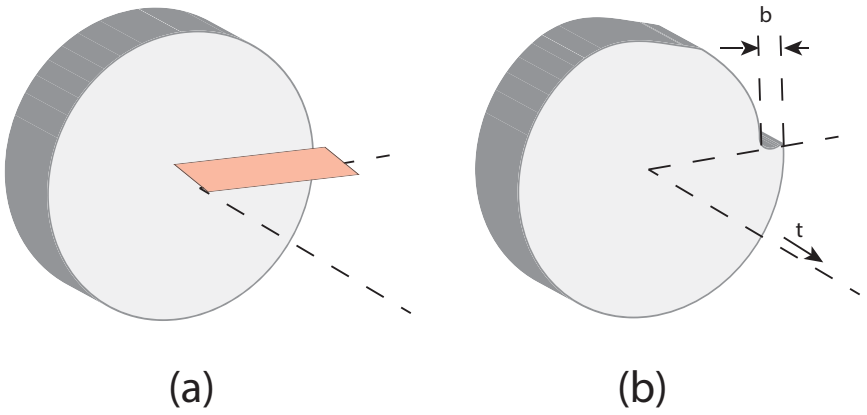

Dislocations are characterized by the nature of the displacement caused by it. The displacement is measured as the *burger's* vector, defined by

$$\mathbf{b} = -\oint_C \frac{\partial \mathbf{u}}{\partial l}\,\mathrm{d}l,$$

where, $\mathbf{u}$ is the elastic displacement caused by the dislocation in the crystal around the dislocation line, ξ. In practice, the measurement of the *burger's* vectoris performed by constructing the burger's circuit. Consider two circular loops, one around the dislocation line and one in a perfect crystal. In both the circuits, the same number of atomic jumps are made along each direction. In the former case around the dislocation line, the loop is closed while in the latter case avoiding the dislocation, the loop is open. The Burger's vector is defined as the vector that closes this loop. The schematics of this method of determining the *burger's* vectoris shown in Figure 4.2.

Figure 4.2: Schematics describing the construction of the burger's circuit and determination of the *burger's* vector, $\mathbf{b}$

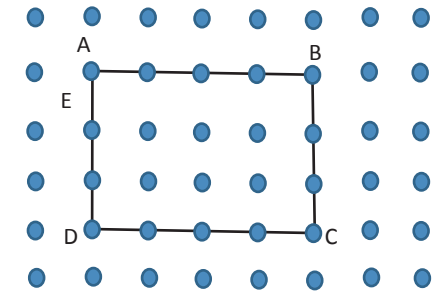

Burger's circuit in a perfect crystal

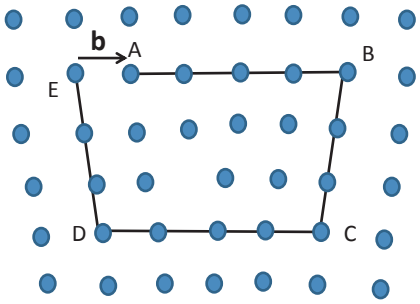

Burger's circuit in a dislocated crystal

Based on the *burger's* vector, dislocations are classified into two types:

1. Edge dislocation

2. Screw dislocation

In the case of an edge dislocation, the *burger's* vector, $\mathbf{b}$ is perpendicular to the dislocation line, ξ, and in the case of a screw dislocation, they are parallel to each other. Hence, by definition:

$$\mathbf{b}.\xi = 0, \qquad \text{for an edge dislocation} \mathbf{b}.\xi = \pm b, \qquad \text{for a screw dislocation} \tag{4.1}$$

In general, experimental observations show the presence of dislocations that are of mixed character, containing both edge and screw components.

In this thesis, we will concern ourselves with the edge dislocation and present ideas

to predict the size of the dislocation-core and its energetics. To this end, first, we present the Continuum treatment of the long-ranged far-field elastic fields arising out of an edge dislocation.

Consider a cylinder containing a *Volterra* edge dislocation, such that the axis of the cylinder coincides with the dislocation line, ξ. Figure 4.1 shows the cylinder that is cut and deformed to produce an edge dislocation of burger's vector $\mathbf{b}$. Periodicity is assumed along the dislocation line to avoid any surface effects. This reduces the problem to a plane strain case. For the given edge dislocation, the differential equation for the Airy's stress function in polar coordinates is:

$$\left(\frac{\partial^2}{\partial r^2}+\frac{1}{r}\frac{\partial}{\partial r}+\frac{1}{r^2}\frac{\partial^2}{\partial \theta^2}\right)^2 \psi = 0, \tag{4.2}$$

subject to the boundary condition,

$$b = -\int_{-\infty}^{\infty} \left(\epsilon_{xx}\left(x,\eta\right) - \epsilon_{xx}\left(x,-\eta\right)\right)\,\mathrm{d}x \qquad\qquad \eta \to 0, \eta > 0, \tag{4.3}$$

$$u_z = 0; \tag{4.4}$$

$$\frac{\partial u}{\partial z} = 0; \tag{4.5}$$

On solving for the partial differential equation, the stresses can be shown to be [5]:

$$\begin{aligned}
\sigma_{rr} =& \sigma_{\theta\theta} = -\frac{\mu b \sin\theta}{2\pi\left(1-\nu\right)r} \\
\sigma_{r\theta} =& \frac{\mu b \cos\theta}{2\pi\left(1-\nu\right)r} \\
\sigma_{zz} =& \nu\left(\sigma_{rr}+\sigma_{\theta\theta}\right) = \frac{\mu b \nu \sin\theta}{\pi\left(1-\nu\right)r} \\
\sigma_{rz} =& \sigma_{\theta z} = 0
\end{aligned} \tag{4.6}$$

The stresses in Cartesian coordinates are given by,

$$\begin{aligned}
\sigma_{xx} =& -\frac{\mu b}{2\pi(1-\nu)}\frac{y(3x^2+y^2)}{(x^2+y^2)^2},\\
\sigma_{xy} =& \frac{\mu b}{2\pi(1-\nu)}\frac{x(x^2-y^2)}{(x^2+y^2)^2},\\
\sigma_{yy} =& \frac{\mu b}{2\pi(1-\nu)}\frac{y(x^2-y^2)}{(x^2+y^2)^2},\\
\sigma_{zz} =& \nu\left(\sigma_{xx}+\sigma_{yy}\right),\\
\sigma_{yz} =& \sigma_{xz}=0.
\end{aligned} \tag{4.7}$$

The strain energy associated with the elastic fields is given by:

$$E_{elastic} = \frac{\mu b^2}{4\pi(1-\nu)}\ln\frac{R}{r_0}, \tag{4.8}$$

where, $E_{elastic}$ is the strain energy per unit length of the dislocation, R and r_0 are the outer and inner radii of the annular region around the dislocation core.

The continuum description of the edge dislocation provides very important insights into the deformation fields associated with it. For instance, the stress and thereby the strain fields decay as $1/r$ which shows that the deformation is long ranged. Also, the strain energy of an edge dislocation diverges logarithmically. This strain energy is limited by the size of the grain size. On the other hand, the strain energy and the stress fields tend to infinity as $r \to 0$. The stresses assume values that are never physically realized close to the defect-core.

The continuum description of an edge dislocation provides very accurate description of the far-field deformation, but fails close to the defect-core. Hence, the dislocation is usually divided in to two regions of interest:*Elastic zone* where continuum description has been found to be very accurate and the *Dislocation-Core*, where continuum description is

invalid. Thus, the generic description of the energetics of the dislocation is given by:

$$E_{disloc} = E_{core} + E_{elastic}$$

where, E_{core} is the dislocation-core energy, $E_{elastic}$ is the elastic component of the line energy given by 4.8. A complete description of the characteristics of the dislocation requires the prediction of the dislocation-core as well as its long-ranged elastic fields. Further sections of this chapter will be devoted towards predicting the energetics of the dislocation-core as well as the effect of deformation on its energetics.

4.2 Dislocation-core

In the previous section, we presented the continuum description of the far field deformation of an edge dislocation. But, close to the defect core, quantum mechanical interactions dominate the physics. In the last decade, given the significant increase in computational resources, there has been significant advances in atomistic description of defects in materials. To this end, a number of interatomic potential based methods have been used to predict the dislocation-core. Such empirical potentials based atomistics calculations are limited to modeling phenomenon that have been used in their design and are not transferable to studying other material properties. This restricts the applicability of interatomic potential based methods in modeling the dislocation-core.

A number of density functional theory based methods have attempted to capture the dislocation-core. While such calculations can be very accurate in capturing the atomic structure of the defect-core, they have not been able to accurately predict the energetics of the dislocation-core. Most electronic structure calculations are implemented in a plane-wave basis whose drawbacks have been described in Chapter 3. The periodicity require-

ment of the plane-wave basis implementations are incompatible with the slow decaying deformation fields associated with the dislocations. To overcome such limitations, quad-core arrangement of dislocations or surfaces are introduced. Such artificial constructs impede the prediction of the dislocation-core energy which is crucial in various atomistically informed methods such as dislocation dynamics.

To this end, we perform electronic structure calculations of an isolated edge dislocation that is in equilibrium with the bulk of the crystal. Here, we take advantage of the real-space implementation of OFDFT wherein, arbitrary boundary conditions can be applied.

We consider a perfect edge dislocation in face-centered-cubic aluminum to determine the dislocation core-size. We align our coordinate system, $X-Y-Z$ axes, along $[1\,1\,0]-[1\,\overline{1}\,1]-[1\,\overline{1}\,\overline{2}]$ crystallographic directions, respectively. We begin by considering a perfect crystal of size $2R\sqrt{2}a_0 \times 2R\sqrt{3}a_0 \times 0.5\sqrt{6}a_0$ where a_0 denotes the lattice parameter and R is an integer-valued scaling factor used to consider a sequence of increasing simulation domain sizes. A perfect edge dislocation with Burgers vector $\mathbf{b} = \frac{a_0}{2}[110]$ is introduced at the center of the simulation domain by removing two consecutive half-planes normal to $[110]$ and applying the continuum displacement fields of an edge dislocation to the positions of atoms. In this work, the displacement fields from isotropic elasticity [5] are employed as anisotropic effects are not strong in aluminum. Upon the application of displacement fields, the geometry of the computational domain is no longer cuboidal, and thus, the use of a finite-element basis which can accommodate complex geometries is crucial to the present study.

In order to simulate a perfect edge dislocation, we hold the positions of the atoms fixed and compute the electronic-structure using orbital-free DFT. We employ Dirichlet boundary conditions on the electronic fields—comprising of electron-density, electrostatic potential and kernel potentials—in the X and Y directions and use periodic boundary con-

ditions along the Z direction. The Dirichlet boundary conditions are determined under the Cauchy-Born approximation, where the values of electronic fields on the Dirichlet boundary are computed from periodic unit-cells undergoing the deformations produced by the edge dislocation. The electronic-structure, thus computed, represents an isolated edge-dislocation in bulk with the electronic-structure perturbations from the edge dislocation vanishing on the Dirichlet boundary. The local real-space formulation of orbital-free DFT and the finite-element basis are key to employing these boundary conditions, which are not possible to realize in Fourier based formulations.

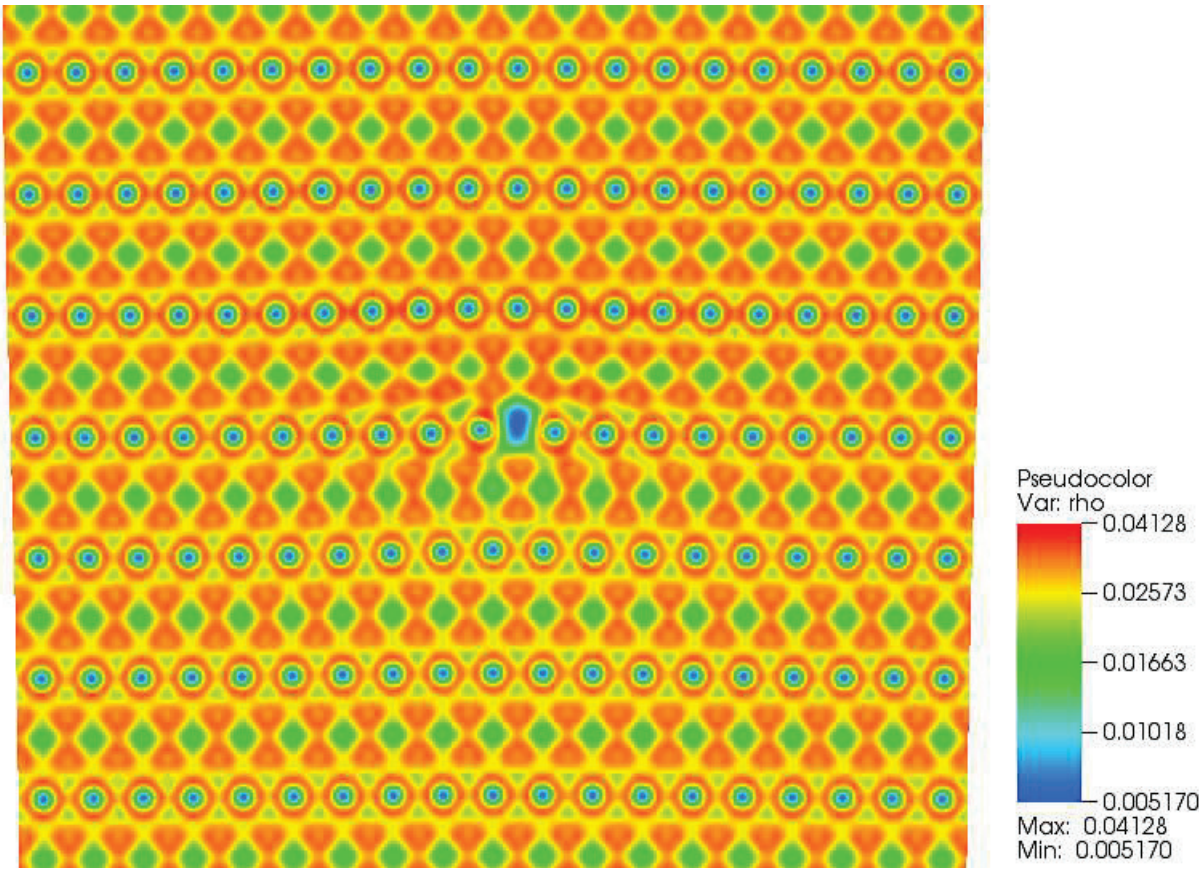

Figure 4.3: Electron-density contours of a perfect edge dislocation in aluminum.

We computed the electronic-structure and ground-state energy of the perfect edge-dislocation for varying simulation domains with $R = 2, 3, 4, 5, 7, 9$. Figure4.3 shows the contours of the electron-density for $R = 5$. We note that a scaling factor R corresponds to

a domain-size where the distance from the dislocation line to the boundary along $[110]$ is $2R|\mathbf{b}|$. The dislocation energy, (E_d), for these various simulation domains is computed as

$$E_d(N,V) = E_{disloc}(N,V) - E_0(N,V) \tag{4.9}$$

where $E_{disloc}(N,V)$ denotes the energy of the N atom system comprising of the dislocation and occupying a volume V, and $E_0(N,V)$ denotes energy of a perfect crystal containing the same number of atoms and occupying the same volume. We first computed the dislocation energy at equilibrium volume (i.e. $V = N\frac{a_0^3}{4}$) for the various domain-sizes considered in this study and the results are presented in Table4.1. Figure 4.4 shows the variation of the dislocation energy with respect to the domain size of the simulation.

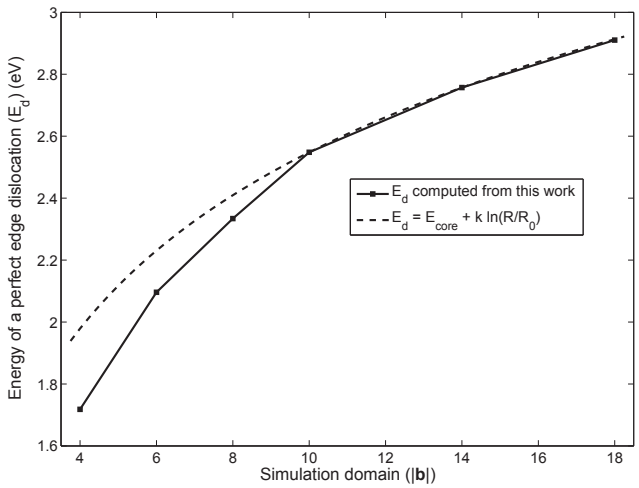

Figure 4.4: Energy of a perfect edge dislocation as a function of simulation domain size

The dislocation energy increases with increasing domain-size, and has an asymptotic logarithmic divergence as expected from continuum theories. In order to understand the extent of electronic relaxations, we considered the change in dislocation energy by increasing the domain-size—for instance, from a domain-size of $2R_1|\mathbf{b}|$ to $2R_2|\mathbf{b}|$—and denote this change by ΔE_d. This change in the dislocation energy has two contributions: (i) the

increase in the elastic energy due to the increase in the domain-size, which we denote by ΔE_{elas}; (ii) electronic contribution from perturbations in the electronic-structure, which we denote by ΔE_{elec}. We computed ΔE_{elas} using the Cauchy-Born hypothesis, where the elastic energy-density at any point is computed from an orbital-free DFT calculation on a unit-cell undergoing the macroscopic deformation produced by the edge dislocation at that point. Upon computing ΔE_{elas}, we infer ΔE_{elec} from ΔE_d ($\Delta E_{elec} = \Delta E_d - \Delta E_{elas}$). The computed ΔE_{elas} and ΔE_{elec} are reported in Table 4.1. It is interesting to note from the results that ΔE_{elec} is comparable to ΔE_{elas} up to a domain-size of $10\mathbf{b}$, suggesting that the electronic-structure perturbations are significant up to distances as far as $10|\mathbf{b}|$ from the dislocation line. This result is in sharp contrast to conventional estimates of core-size to be 1-3$|\mathbf{b}|$, and underscores the need to consider large simulation domains to accurately compute the energetics of dislocations. In the remainder of this work, we consider $10|\mathbf{b}|$ to be the core-size of edge dislocation, and the dislocation energy corresponding to this core-size as the dislocation core-energy. For a perfect edge dislocation, the computed core-energy is 2.548 eV.

Table 4.1: Computed dislocation energy of perfect edge dislocation in aluminum for varying domain-sizes, where N denotes the number of atoms in the simulation domain. ΔE_f denotes the change in the dislocation energy from the previous domain-size, and ΔE_{elas} and ΔE_{elec} denote the elastic and electronic contributions to ΔE.

Simulation domain	N (atoms)	E_f (eV)	ΔE_f (eV)	ΔE_{elas} (eV)	ΔE_{elec} (eV)
$4\|\mathbf{b}\|$	179	1.718	-	-	-
$6\|\mathbf{b}\|$	413	2.096	0.378	0.230	0.148
$8\|\mathbf{b}\|$	743	2.334	0.237	0.164	0.073
$10\|\mathbf{b}\|$	1169	2.548	0.215	0.118	0.097
$14\|\mathbf{b}\|$	2309	2.757	0.209	0.187	0.022
$18\|\mathbf{b}\|$	3833	2.91	0.153	0.156	-0.003

4.3 Shockley Partials

Plastic deformation in crystalline materials is realized by the movement of the dislocation through gliding across the slip plane containing the dislocation line along the burger's vector. In the case of a perfect edge dislocation, such a slip motion would require a displacement of atleast one unit lattice vector ($\mathbf{b}$) whose gliding path across slip plane can be energetically penalizing. Instead of moving both the half planes, a better glide path could be obtained by moving the half planes individually [5]. Such a glide path would require the half-planes to be separated by an intrinsic stacking fault. This arrangement or splitting of the perfect edge dislocation into partials which are glissile on the same slip plane are called the *Shockley partials*. The Shockley partials are split from the perfect edge dislocation such that:

$$\mathbf{b} = \mathbf{b}_1 + \mathbf{b}_2.$$

The split into partials is determined by the Frank's energy criterion:

$$|\mathbf{b}_1|^2 + |\mathbf{b}_2|^2 < |\mathbf{b}|^2 \tag{4.10}$$

In the case of a perfect edge dislocation in FCC crystals, they usually split into:

$$\frac{a_0}{2}[110] = \frac{a_0}{6}[21\bar{1}] + \frac{a_0}{6}[121] \tag{4.11}$$

Experiments using X-ray diffraction techniques report the presence of Shockley partials rather than a perfect edge dislocation as they are more energetically favourable. The partial separation distance is determined by the stacking fault energy of the material. Higher the stacking fault, smaller is the partial separation distance, as is the case with Aluminum and vice versa. Atomistic calculations also support such a reaction which is realized by

allowing the atoms in the dislocation-core to relax.

As a next step in our study, we allowed for internal atomic relaxations in the simulation domain corresponding to $10|\mathbf{b}|$ by holding the positions of atoms fixed on the boundary. Upon atomic relaxations, the perfect edge dislocation split into Shockley partials. Figure 4.5 shows the edge component of the differential displacements and indicates the location of the Shockley partials. The partial separation distance computed from the edge-component differential displacement plot is 12.8 $\mathring{A}$ $(4.5|\mathbf{b}|)$. This is in good agreement with other DFT studies which have reported partial separation distances between 9.5-13.7 $\mathring{A}$ [82, 84]. Table 4.2 tabulates the various reported values in literature along with our study. The core-energy of Shockley partials is computed to be 1.983 eV, or, equivalently, the core-energy per unit dislocation line is 0.401 $eV/\mathring{A}$.

Table 4.2: Shockley partial separation distance

	Partial Separation distance (Å)
Experiment (WB-TEM) [91]	8.0
OFDFT (Real-space)	12.8
OFDFT (Plane-wave) [19]	13.7
FP-GFBC [20]	7.0-9.5
EAM [92, 93]	5-15

Thus far, we have studied an isolated edge dislocation in equilibrium with the bulk of the material. From our studies, we have predicted the size of the dislocation-core to be $10\,|\mathbf{b}|$. The energy of a perfect edge dislocation is computed to be 0.515 $eV/\mathring{A}$. Upon atomic relaxation, the perfect edge dislocation dissociates into Shockley partials with a partial separation distance of 12.8 $\mathring{A}$ and a line energy of 0.401 $eV/\mathring{A}$.

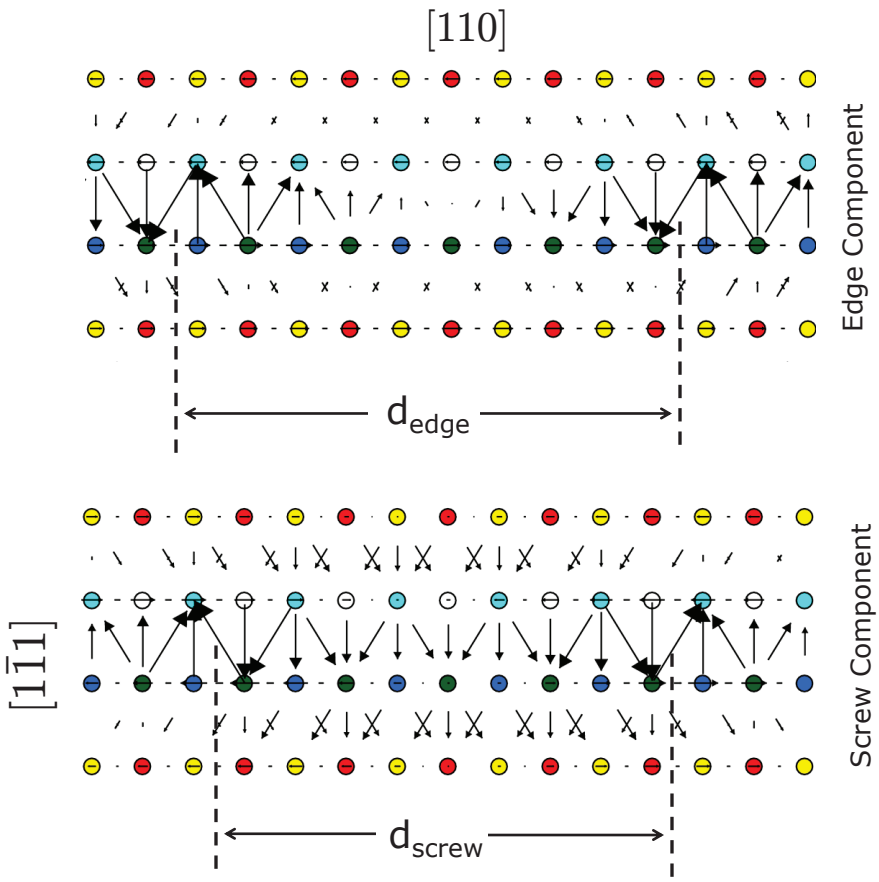

Figure 4.5: Differential displacement plot of the edge and screw component of Shockley partials. The dotted lines represent the location of the partials, and d_{edge} denotes the partial separation distance.

4.4 Effect of volumetric deformations on dislocation core-energy

The dislocation-core energy is usually considered to be an inconsequential constant in simulations involving interaction of dislocations. Simulations involving dislocation interactions are mostly concerned with the effect of external stresses on the energetics of the dislocation rather than the energy of the dislocation itself [85]. This is partly due to lack of available data from electronic structure calculations. Recent studies on point defects [86, 94] which demonstrated that volumetric deformations can significantly influence defect-core energies.

To this end, we imposed macroscopic volumetric strains of -5%, -2%, -1%, 1%, 2% and 5%, and computed the relaxed core-structure and core-energy of Shockley partials as a function of the imposed volumetric strains. For the range of volumetric strains considered, the partial separation distance in terms of $|\mathbf{b}|$ was found to be insensitive to volumetric strain, and is $\sim 4.5|\mathbf{b}|$. However, the computed core-energy demonstrated a dependence on volumetric strain, and is shown in figure 4.6. The core-energy (per unit dislocation line) changed from 0.48 $eV/\mathring{A}$ at -5% volumetric strain to 0.34 $eV/\mathring{A}$ at 5% volumetric strain, and this change corresponds to a significant fraction (~ 0.3) of the core-energy at equilibrium. This finding is in sharp contrast to the assumption that the core-energy of a dislocation is an inconsequential constant. Interestingly, the slope of the core-energy dependence on volumetric strain is non-zero, and in fact maximum, at zero volumetric strain. This suggests that the energetics of dislocation-cores have a non-trivial role in governing the behavior of dislocations even at small strains and at macroscopic scales.

In order to elucidate the role of dislocation core-energy in influencing dislocation behavior, we consider the force on a unit dislocation line segment resulting from external

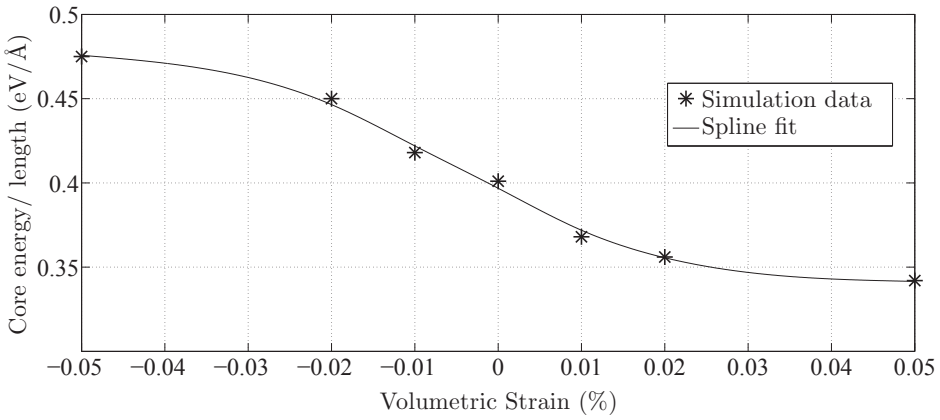

Figure 4.6: Core-energy per unit dislocation line of relaxed Shockley partials as a function of macroscopic volumetric strain.

loads or other defects. This force has two parts, the classical Peach-Koehler force corresponding to elastic interactions given as [95]

$$\mathbf{f}^{PN} = (\sigma.\mathbf{b}) \times \xi,$$

and force due to the core-energy dependence on volumetric strains (referred to as core-force), given by

$$\mathbf{f}^{core}_{\epsilon_v} = -\frac{\partial E_{core}}{\partial \epsilon_v} \nabla \epsilon_v,$$

where ϵ_v denotes the volumetric strain and $\frac{\partial E_{core}}{\partial \epsilon_v}$ is computed from figure 4.6. It is interesting to note that, while the Peach-Koehler force depends on the stress-tensor (which is related to the strain-tensor), the core-force, which has been ignored thus far, depends on the gradient of strain-tensor and can be significant in regions of inhomogeneous deformations.

In order to understand the relative importance and implications of these core-effects on dislocation behavior, we consider the interaction force between dislocation dipoles in two specific cases as shown in figure 4.7: Case (i) where the dislocations are located at $(X, Y) = (0, 0)$ with Burgers vector $\frac{a_0}{2}[110]$ and another dislocation also along $Z-$axis located at $(X, Y) = (r, 0)$ with Burgers vector $-\frac{a_0}{2}[110]$ and Case (ii) where the dislocations

are located at $(X, Y) = (0, 0)$ and the other dislocation located at $(X, Y) = (r/\sqrt{2}, r/\sqrt{2})$

.

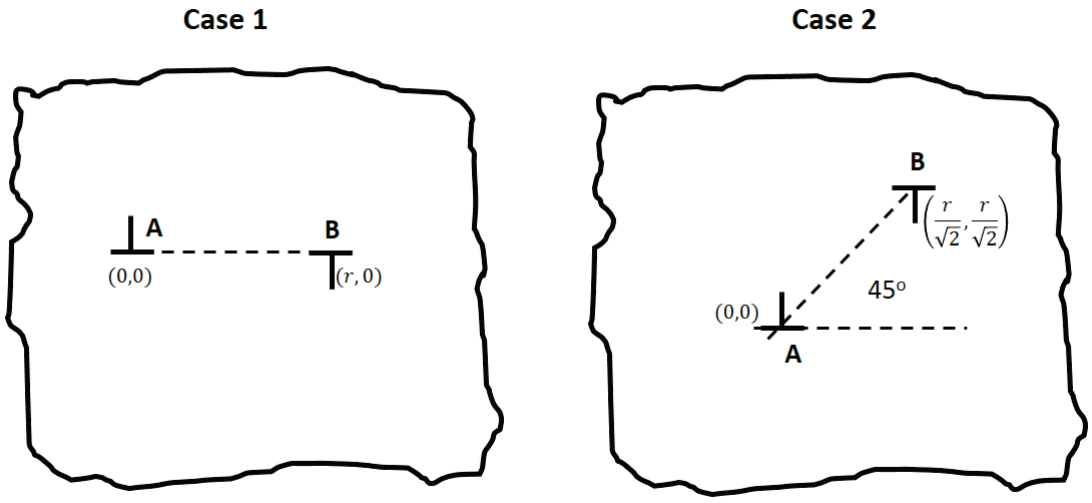

Figure 4.7: Schematics for the two scenarios considered. Case (i): Edge dislocations aligned along the glide plane. Case (ii): Dislocations at an angle of 45^o

Case (i): The Peach-Koehler force on the dislocation is given by:

$$\mathbf{f}^{PN} = -\frac{\mu b^2}{2\pi(1-\nu)}\frac{1}{r}\hat{\mathbf{i}},$$

Using the elastic fields from equation 4.7, the core-force can be shown to be

$$\mathbf{f}^{core}_{\epsilon_v} = -2\frac{\partial E^{core}}{\partial \epsilon_v}\bigg|_{\epsilon_v=0} \nabla\epsilon_v = -2\frac{\partial E^{core}}{\partial \epsilon_v}\bigg|_{\epsilon_v=0} \frac{\mu b}{\pi(\lambda+2\mu)}\frac{1}{r^2}\hat{\mathbf{j}}.$$

Case (ii): The Peach-Koehler force on the dislocation is given by:

$$\mathbf{f}^{PN} = -\frac{\mu b^2}{2\pi(1-\nu)}\frac{\sqrt{2}}{r}\hat{\mathbf{j}},$$

and the core-force is:

$$\mathbf{f}^{core}_{\epsilon_v} = -2\frac{\partial E^{core}}{\partial \epsilon_v}\bigg|_{\epsilon_v=0} \nabla\epsilon_v = -2\frac{\partial E^{core}}{\partial \epsilon_v}\bigg|_{\epsilon_v=0} \frac{\mu b}{\pi(\lambda+2\mu)}\frac{1}{r^2}\hat{\mathbf{i}},$$

where, λ is the Lame's parameter.

The Peach-Koehler force arising from dislocation interactions is known to be $O(\frac{1}{R})$ [5], where R denotes the distance between the dislocations. On the other hand, the core-force is $O(\frac{1}{R^2})$ which follows from the $O(\frac{1}{R})$ decay of the volumetric strain produced by a dislocation. In the first case, where the dislocations are aligned along the glide plane, the Peach-Koehler force corresponds to a glide force on the dislocations, whereas the core-force corresponds to a climb force. In the second case, the Peach-Koehler force corresponds to a climb force, whereas the core-force corresponds to a glide force. Using $\frac{\partial E_{core}}{\partial \epsilon_v}|_{\epsilon_v=0}$ computed from figure 4.8, we estimated the magnitude of the core-force in the second case and compared it to the Peierls-Nabarro force—the force that will cause dislocation glide.

Choosing the Peierls stress to be $1.6\ GPa$ [96], it is striking to note that even at a distance of $20nm$ between the dislocations the core-force is equal to or greater than the Peierls-Nabarro force. Further, even up to $60nm$ the core-force is greater than 10% of the Peierls-Nabarro force. These results suggest that the force contribution arising from core-effects, which has been ignored thus far, can play a significant role in governing the behavior of dislocations, especially in regions of inhomogeneous deformations.

4.5 Summary

To conclude, the present study employed a real-space finite-element discretization of orbital-free DFT to perform electronic structure calculations of an isolated edge dislocation in equilibrium with the bulk. Based on estimating the contribution from electronic-structure

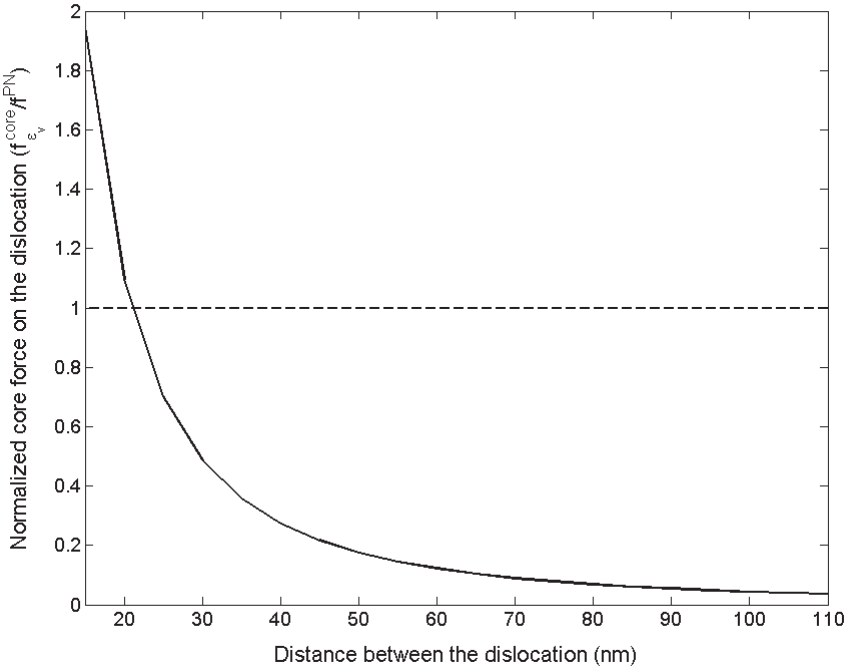

Figure 4.8: The core-force in Case (ii) normalized with respect to the Peierls-Nabarro force as a function between the two dislocations

effects to the energetics of the dislocation, we calculated the size of the dislocation-core to be $10\,|\mathbf{b}|$, which is much larger than conventional estimates that have been widely used thus far. Upon the relaxation of the nuclei, the perfect edge dislocation split into Shockley partials separated by a distance of $12.8\mathring{A}$ which is in good agreement with other DFT computations. More importantly, the core-energy of Shockley partials was found to be significantly dependent on macroscopic volumetric strains. This core-energy dependence on volumetric strains results in a short-range force on dislocations, especially in regions of inhomogeneous deformations, which is found to be significant up to tens of nanometers and can play an important role in governing dislocation behavior.

CHAPTER 5

Vacancy clustering and dislocation loops

Quenching of metals is a very common technique after hot-working in various manufacturing procedures. One of the most widely observed phenomenon is the clustering of vacancies in R-dislocation loops or prismatic dislocation loops (dislocation loops whose Burgers vector has a component normal to their plane) in such quenched-in specimens [97] which can result in significant loss of strength of materials. Similar embrittlement of metals have also been observed in metals subjected to radiation [98, 99]. As the irradiation dose increases, displacement cascades are observed which leads to defects in the material. Beyond a threshold of radiation, a significant population of prismatic dislocation loops have been experimentally observed to arise in metals. Such phenomena have far-reaching consequences in design of nuclear reactors. Various interatomic potentials based simulations have been performed to study radiation induced damage in materials [100, 101, 102, 103, 104]. It is of considerable importance to study the mechanism by which these dislocation loops nucleate, as the formation of such defects results in a rapid deterioration of material properties, especially fracture toughness.

5.1 Mono and di-vacancy in Aluminium

In Chapter 3, we presented the mono and di-vacancy studies in Aluminium in the context of cell-size studies impressing on the need to perform large cell-size calculations corresponding to realistic concentrations of defects. The simulations in Chapter 3 were performed using Goodwin-Heine-Needs pseudo potential. In the recent past since those studies were performed, more accurate pseudo-potentials that work better with the density-dependent kinetic energy functionals were developed. One such pseudo-potential that has shown great promise is the Bulk Local Pseudo potential (BLPS) [105]. In keeping pace with the recent advances, we have used the BLPS pseudo potential for all the simulations in this chapter.
We repeat the mono and di-vacancy calculations with dirichlet boundary conditions on the simulation cell, wherein, the nuclei on the boundaries are held fixed while the electronic fields are as determined by the bulk. We perform the calculations in various cell-sizes and compute the binding energies of the di-vacancies using equation 3.51 for various cell-sizes. Numerical parameters are chosen such that the errors in the computed formation energies do not exceed $0.01\ eV$. The formation energy of a mono-vacancy in Aluminum is calculated as $0.72\ eV$.

Figure 5.1 shows the cell-size effect in the binding energy of di-vacancies when BLPS pseudo-potential is used. The results show that we need $10^3 - 10^4$ atoms to get converged binding energies. The $< 100 >$ and $< 110 >$ di-vacancy binding energies are computed to be $0.045\ eV$ and $0.067\ eV$ respectively. The positive binding energy shows that the di-vacancies are attractive and energetically favourable compared to two isolated mono-vacancies. We note that the cell-size effects are reduced while using the BLPS pseudo potential compared to the Goodwin-Heine-Needs pseudo potential, but still close to 4000 atoms are required which necessitates the need to use coarse graining techniques.

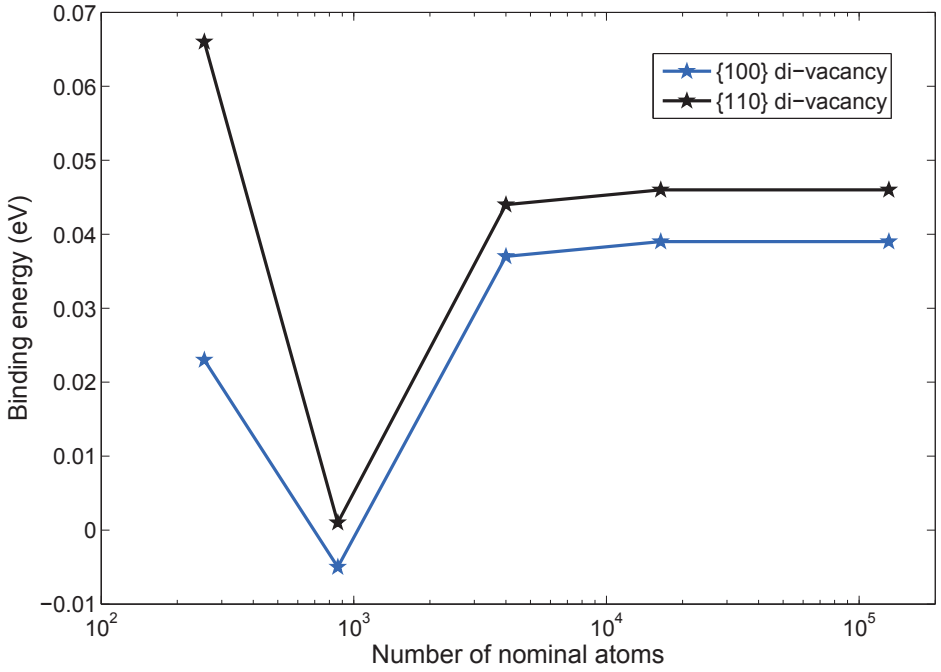

Figure 5.1: Cell size study of binding energies of di-vacancies in $< 110 >$ and $< 100 >$ directions in aluminium

5.2 Quad-vacancies

Having established the stability of di-vacancies, we proceed further to investigate vacancy clustering mechanism by predicting the energetics of quad-vacancies. To this end, we study the quad-vacancy formations wherein each vacancy has two other vacancies as nearest or second nearest neighbors. Similar to the studies performed for the mono and di-vacancies, we perform cell-size studies for quad-vacancies.

Figure 5.2 shows the cell-size study of formation energy of a $\{100\}$ planar quad-vacancy in aluminium. The study shows that we need close to 10^4 atoms to obtain convergence with respect to formation and correspondingly binding energies. Table 5.1 shows the binding energies of the different configurations of quad-vacancies calculated from studies performed on cell-sizes of the order of 10^4 atom.

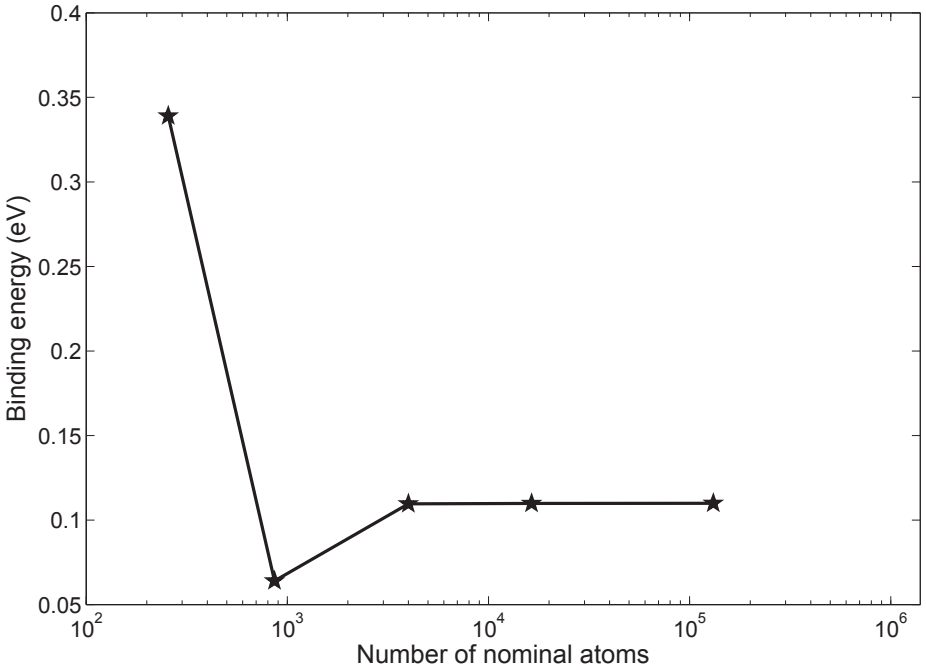

Figure 5.2: Cell size study of vacancy binding energy of quad-vacancy in $\{100\}$ plane given by the third configuration in table 5.1

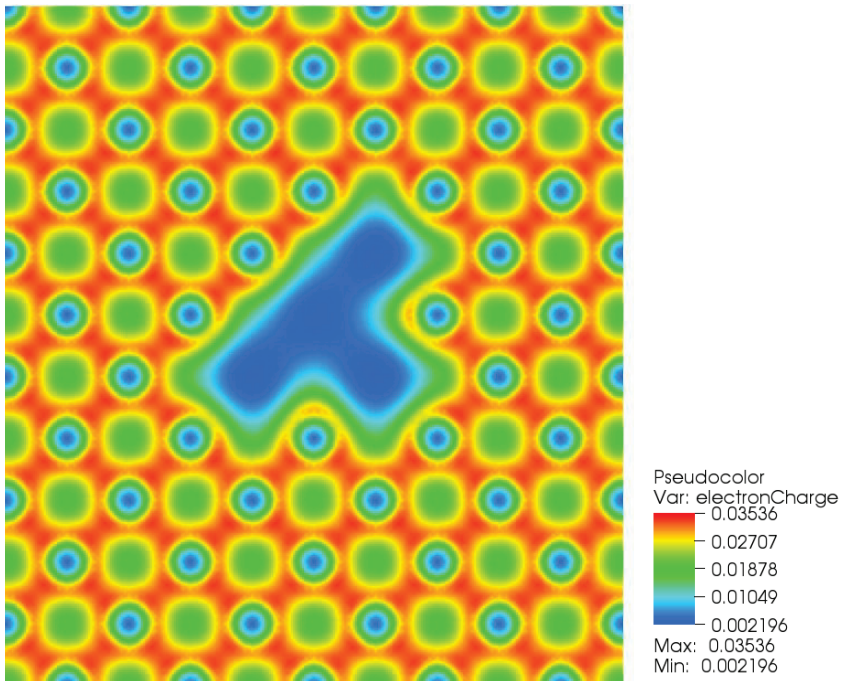

Figure 5.3: Electron-density contours of quad vacancies in $\{100\}$ plane given by the third configuration in table 5.1

Table 5.1: Binding energy of quad-vacancies in aluminium

Structure	Vacancy positions	Vacancy binding energy (eV)
Planar $\{100\}$	(0,0,0), (a/2,a/2,0), (a,0,0), (a/2,-a/2,0)	0.08
Planar $\{100\}$	(0,0,0), (a/2,a/2,0), (a,0,0), (3a/2,a/2,0)	0.1
Planar $\{100\}$	(0,0,0), (a/2,a/2,0), (a,0,0), (a,a,0)	0.1
Planar $\{100\}$	(0,0,0), (a,0,0), (0,a,0), (a,a,0)	0.22
Planar $\{110\}$	(0,0,0), (0,a/2,a/2), (a,0,0), (a,a/2,a/2)	0.3
Planar $\{111\}$	(0,0,0), (0,a/2,a/2), (a/2,a/2,0), (a/2,a,a/2)	0.33
Non Planar	(0,0,0), (0,a/2,a/2), (a/2,0,a/2), (a/2,a/2,0)	0.55
Non Planar	(0,0,0), (a,0,0), (a/2,a/2,0), (a/2,0,a/2)	0.31
Non Planar	(0,0,0), (a,0,0), (a/2,a/2,0), (0,a/2,a/2)	0.23

Of particular interest are the quad-vacancies in $\{111\}$ and $\{110\}$ planes. Figures 5.3 and 5.4 show the electron density contours of quad vacancies in $\{111\}$ and $\{110\}$ planes respectively. Experiments show that these planes are the most likely habit planes for the clustering of much larger number of vacancies eventually resulting in formation of dislocation loops. Table 5.1 shows that the binding energy of quad-vacancies are far more stable than two di-vacancies pointing to the possibility of di-vacancies combining to form quad-vacancies in $\{111\}$ and $\{110\}$ planes.

5.3 Hexagonal vacancy loops in $\{111\}$

As stated earlier, the clustering of vacancies in $\{111\}$ plane could potentially lead to formation of dislocation loops. It is hypothesized that when the number of vacancies are large enough, the planes of atoms above and below the vacancies could potentially collapse to create more stable dislocation loops. Experimental observations show that the $\{111\}$ is the most likely plane of habitat for dislocation loops. In particular, loops of symmetric shapes close to that of a hexagon have been observed. But, the loops are found to consist of as many of $50 - 100$ vacancies. While such large loops have been observed, the intermediate mechanisms involved in such loop formation consisting of fewer vacancies are hard to ob-

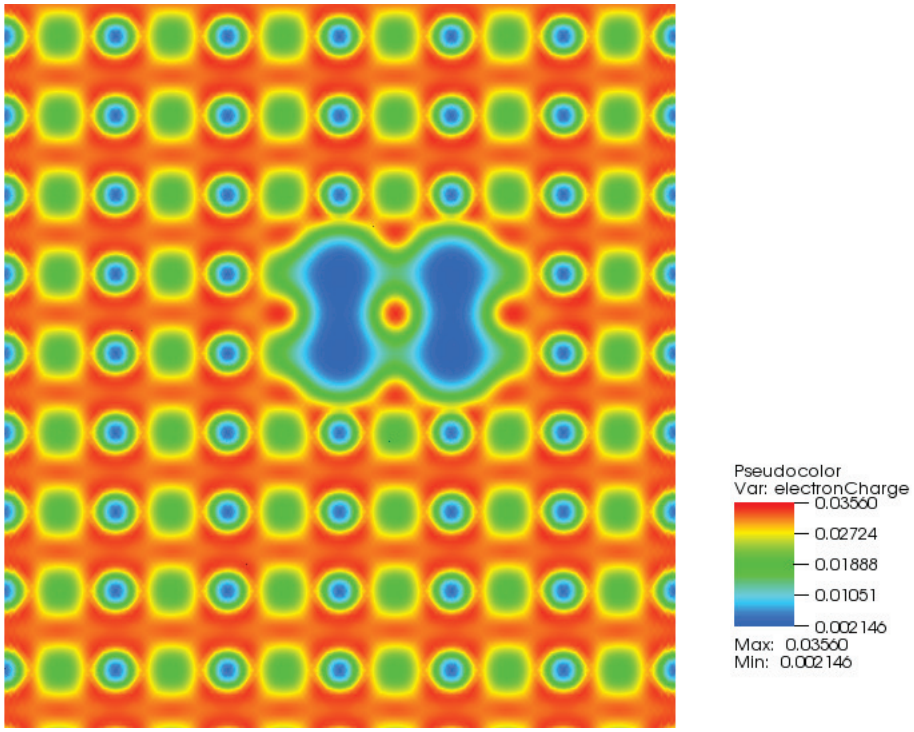

Figure 5.4: Electron-density contours of quad vacancies in $\{110\}$ plane

serve. In this work, we study vacancy loops consisting of 7 and 19 vacancies in the $\{111\}$ plane.

Figure 5.5 shows the electron density contours of an unrelaxed vacancy loop in $\{111\}$ plane consisting of 7 vacancies. The formation energy of the vacancy loop is $4.765\ eV$ with a binding energy of $0.29\ eV$. While the vacancy loop is stable with a positive binding energy, the surrounding plane of atoms do not collapse to form a dislocation loop. We note that a previous study performed using Thomas-Fermi-weizacker model of kinetic energy potentials predicted such a stable relaxed configuration [106].

Proceeding further with our investigation, we increase the number of vacancies to 19. The number of vacancies are chosen such that they create a symmetrical hexagonal shaped vacancy loop similar to the seven vacancy loop.

Figure 5.6 shows the electron density contours of the unrelaxed hexagonal vacancy loop in Aluminium. The unrelaxed formation energy of the 19 vacancy loop is given by 15.22

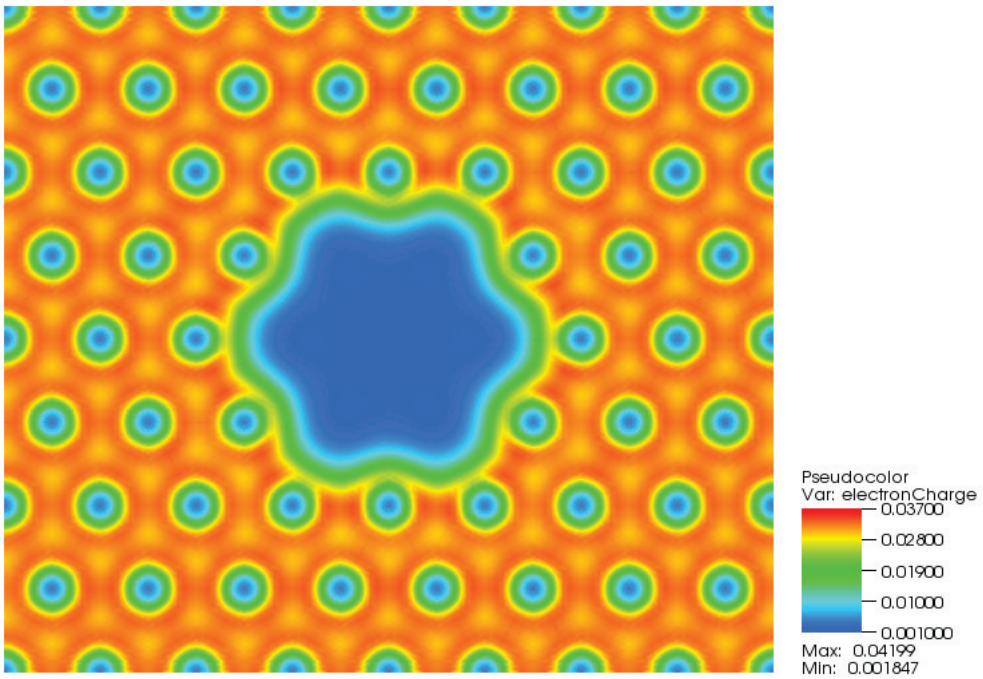

Figure 5.5: Electron-density contours of unrelaxed hexagonal 7 vacancy loop in $\{111\}$ plane

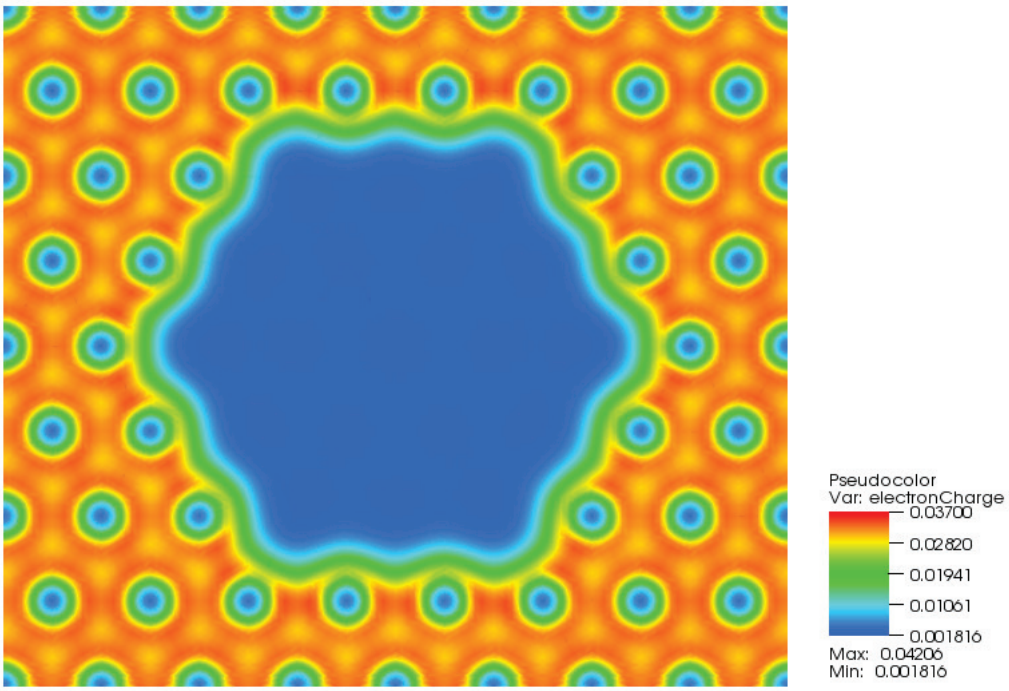

Figure 5.6: Electron-density contours of unrelaxed hexagonal 19 vacancy loop in $\{111\}$ plane

eV. On allowing relaxation in a million atom cell, we see the planes above and below the vacancy loop collapse to form a dislocation loop. The formation energy of the vacancy loop is $3.712\ eV$ with a binding energy of $10.015\ eV$ which points to a strong tendency of the vacancies to cluster together and collapse to form a stable dislocation loop. The major component of the collapse of the planes surrounding the vacancy loop is along $< 111 >$ direction, which is perpendicular to the loop. In addition to the perpendicular collapse, the planes also slip along the $< 112 >$ and $< 110 >$ directions. The slip along the $< 112 >$ direction is of particular importance. While the collapse along the $< 111 >$ direction creates a dislocation loop, it also encloses a stacking fault which are energetically penalizing. Experiments show that dislocation loops of size 50 Åusually slip along $< 112 >$ direction to eliminate the stacking fault and in the process, create a perfect edge dislocation loop. The slip observed in the 19 vacancy loop is not complete enough to null the stacking fault from the $< 111 >$ collapse. A complete slip may be observed as the number of vacancies clustering increases along with the size of the stacking fault area. The burger's vector, based on the displacement fields of the collapsed loop, is calculated as ($\frac{1}{3}[111]$, $\frac{1}{18}[11\hat{2}]$, $\frac{1}{13}[1\hat{1}0]$). We note that the electronic perturbations receded with a cell-size of 10^4 atoms while we needed a million atom cell to compute the elastic work done by the dislocation loop.

5.4 Summary

In this chapter, we have investigated vacancy clustering by predicting the energetics of mono, di and quad vacancies in different planes. The investigations shows that di and quad vacancies, especially quad vacancies in the $\{110\}$ and $\{111\}$ planes are attractive and stable. Further, informed from experimental observations, we predicted the energetics of

hexagonal vacancy clusters in $\{111\}$ plane. While the 7 vacancy cluster does not show any collapse to create a dislocation loop, it is still stable and attractive. In the case of the 19 vacancy cluster, the planes surrounding the vacancies collapse to create a dislocation loop. The binding energy of this dislocation loop is far greater than any other vacancy cluster with fewer vacancies indicating a strong tendency of the vacancies to cluster and create large dislocation loops in the material. Also, the planes tend to slip along $< 112 >$ direction towards a stacking fault free perfect dislocation loop. While the slip was not complete in the 19 vacancy loop, we suspect that such a displacement occurs in larger vacancy loops as evidenced in experiments.

CHAPTER 6

Conclusion and future work

6.1 Summary

This dissertation presents a comprehensive method to study defects in metals, whose electronic structure is close to that of a free electron gas, that are in chemical equilibrium with the rest of the bulk of material. To this end, the work presented in this thesis can be summarized as follows:

- *Local variational formulation*: Recent advances in the modeling of kinetic energy functionals have given rise to non-local functionals in orbital free density functional theory. As a first step, the non-local kinetic energy functionals were reformulated into local formulations using variational principles. The local formulation of the orbital free density functional theory was implemented in a finite element basis and benchmark bulk properties were computed which compared well with the plane-wave basis implementations.

- *Coarse graining OFDFT*: The local reformulation developed for the non-local kinetic energy functionals paved the way for their implementation in the Quasi-Continuum framework. Previously, the coarse graining technique was introduced in the context of Thomas-Fermi-Weizacker family of kinetic energy functionals. In this work, the

coarse graining techniques were extended to include any class of non-local kinetic energy functionals. The coarse graining techniques were then used in studying the cell-size effects of mono and di-vacancies in Aluminium. Results show that cell-sizes corresponding to realistic concentrations are required to capture the energetics of defects.

- *Edge dislocations*: The local real-space formulation of the orbital free density functional theory is used to predict the energetics of an isolated edge dislocation in Aluminium. The local formulation in combination with a finite element basis implementation allows for application of mixed boundary conditions as required by the long-ranged elastic fields of the edge dislocation. Based on the electronic contribution to the energy of the dislocation in comparison with the elastic work done in each annular region, we compute the size of the dislocation-core to be $10\,|\mathbf{b}|$. Traditional estimates of the core-size have been around $1-3\,|\mathbf{b}|$. The full-edge dislocation, on atomic relaxation, dissociates into Shockley partials separated by a stacking fault of width $12.8\mathring{A}$. Investigating further, we find that the volumetric strain has a significant influence on the dislocation-core energy. This leads to a core-force when a dislocation is subjected to an external load. This core-force is a short-ranged force which varies as $O(\frac{1}{r^2})$. When considering the interaction between dislocation dipoles, the core-force can cause gliding at distances smaller than 20 nm and is greater than 10 $\%$ of the Peierls-Naborro force at distances smaller than 60 nm.

- *Vacancy clustering*: The coarse graining techniques are used to predict the energetics of vacancy clusters in Aluminium. Results of studies on di and quad vacancies show that the binding energies are positive. This implies that the di and quad vacancies are energetically favorable. In particular, planar quad vacancies in $\{110\}$ and

$\{111\}$ planes are the more stable than di-vacancies supporting vacancy clustering mechanisms. On further investigation of vacancy cluster in $\{111\}$ plane, prismatic dislocation loops are formed with 19 vacancies. This dislocation loop has a binding energy of $10\ eV$ which shows that such loops are far more energetically favorable compared to any other clusters with fewer vacancies.

6.2 Future direction

The results of the study of defects in Aluminium show the need to perform large cell-size calculations as well as the effect on external deformations on the defect-core energetics. The results also point to application of appropriate boundary conditions on the simulation cell-size that simulates the defect in equilibrium with the bulk of the material. Motivated by the results shown in the previous chapters, following paths could be pursued to further understand the energetics of defects in Aluminium:

- *Effect of deviatoric strain on dislocation-core*: While studies performed in this work have shown the effect of volumetric strain on the dislocation-core energetics, other components of the strain tensor haven't been studied and understanding their influence could help in further improving the modeling of plastic deformation in metals.

- *Solute hardening or softening*: Dislocation cores have been observed to act as sinks for point defects such as vacancies and interact with other solute atoms. Such interactions are suspected to be the cause for hardening or softening of the metal. Investigations related to the energetics of such interactions could pave the way for quantitatively predicting the rate of hardening or softening in metals

- *Influence of an approaching crack tip*: Our calculations show that $\{111\}$ plane dislocation loops are very stable. From DFT calculations as well as experiments, we

know that the $\{111\}$ plane has the least surface energy making it the most probable plane to have a crack-tip. An approaching crack tip could influence the energetics of the dislocation loop through its deformation fields. The energetics of the dislocation loop could be used to compute the energy release rate of an approaching crack tip.

The real-space local formulation affords the ability to apply arbitrary boundary conditions which greatly aid the modeling of defects with long ranged elastic fields. The coarse graining techniques provides the ability to simulate in large enough cell-sizes to capture the defect-core energetics. This coarse graining technique can be applied to gain fundamental insights into deformation and failure mechanisms in crystalline solids.

BIBLIOGRAPHY

[1] Govind, N. and Carter, E., "Orbital-free kinetic-energy functionals for the nearly free electron gas," *Physical Review B*, Vol. 58, 1998, pp. 13–465.

[2] Choly, N. and Kaxiras, E., "Kinetic energy density functionals for non-periodic systems," *Solid state communications*, Vol. 121, No. 5, 2002, pp. 281–286.

[3] Gavini, V. and Liu, L., "A homogenization analysis of the field theoretic approach to the quasi-continuum method," *Journal of the Mechanics and Physics of Solids*, Vol. 59, No. 8, 2011, pp. 1536–1551.

[4] Phillips, R., *Crystals, defects and microstructures: modeling across scales*, Cambridge University Press, 2001.

[5] Hirth, J. P. and Lothe, J., "Theory of dislocations." *John Wiley and Sons, Inc., 1982,*, 1982, pp. 857.

[6] Trinkle, D. R. and Woodward, C., "The chemistry of deformation: How solutes soften pure metals," *Science*, Vol. 310, No. 5754, 2005, pp. 1665–1667.

[7] Hull, D. and Bacon, D. J., *Introduction to dislocations*, Vol. 257, Pergamon Press Oxford, 1984.

[8] Tadmor, E. B., Ortiz, M., and Phillips, R., "Quasicontinuum analysis of defects in solids," *Philos. Mag. A*, Vol. 73, 1996, pp. 1529–1563.

[9] Kelchner, C. L., Plimpton, S. J., and Hamilton, J. C., "Dislocation nucleation and defect structure during surface indentation," *Phys. Rev. B*, Vol. 58, 1998, pp. 11085–11088.

[10] Gumbsch, P. and Gao, H., "Dislocations Faster than the Speed of Sound," *Science*, Vol. 283, 1999, pp. 965–968.

[11] Li, J., Vliet, K. J. V., Zhu, T., Yip, S., and Suresh, S., "Atomistic mechanisms governing elastic limit and incipient plasticity in crystals," *Nature*, Vol. 418, 2002, pp. 307–310.

[12] Marian, J., Cai, W., and Bulatov, V. V., "Dynamic Transitions from Smooth to Rough to Twinning in Dislocation Motion," *Nature Materials*, Vol. 3, 2004, pp. 158–163.

[13] Marian, J., Knap, J., and Ortiz, M., "Nanovoid Cavitation by Dislocation Emission in Aluminum," *Phys. Rev. Lett.*, Vol. 93, 2004, pp. 165503.

[14] Eidelman, S., Hayes, K., Olive, K. e., Aguilar-Benitez, M., Amsler, C., Asner, D., Babu, K., Barnett, R., Beringer, J., Burchat, P., et al., "Review of particle physics," *Physics Letters B*, Vol. 592, No. 1, 2004, pp. 1–5.

[15] Finnis, M., *Interatomic forces in condensed matter*, Vol. 1, Oxford University Press, 2003.

[16] Parr, R. G. and Yang, W., *Density-functional theory of atoms and molecules*, Vol. 16, Oxford university press, 1989.

[17] Fago, M., Hayes, R. L., Carter, E. A., and Ortiz, M., "Density-functional-theory-based local quasicontinuum method: Prediction of dislocation nucleation," *Physical Review B*, Vol. 70, No. 10, 2004, pp. 100102.

[18] Choly, N., Lu, G., Weinan, E., and Kaxiras, E., "Multiscale simulations in simple metals: A density-functional-based methodology," *Physical Review B*, Vol. 71, No. 9, 2005, pp. 094101.

[19] Shin, I., Ramasubramaniam, A., Huang, C., Hung, L., and Carter, E. A., "Orbital-free density functional theory simulations of dislocations in aluminum," *Philosophical Magazine*, Vol. 89, No. 34-36, 2009, pp. 3195–3213.

[20] Woodward, C., Trinkle, D., Hector Jr, L., and Olmsted, D., "Prediction of dislocation cores in aluminum from density functional theory," *Physical review letters*, Vol. 100, No. 4, 2008, pp. 045507.

[21] Gavini, V., Bhattacharya, K., and Ortiz, M., "Quasi-continuum orbital-free density-functional theory: A route to multi-million atom non-periodic DFT calculation," *Journal of the Mechanics and Physics of Solids*, Vol. 55, No. 4, 2007, pp. 697–718.

[22] Ziman, J. M., *Principles of the Theory of Solids*, Cambridge University Press, 1972.

[23] Hohenberg, P. and Kohn, W., "Inhomogeneous electron gas," *Physical review*, Vol. 136, No. 3B, 1964, pp. B864.

[24] Kohn, W. and Sham, L. J., "Self-consistent equations including exchange and correlation effects," *Physical Review*, Vol. 140, No. 4A, 1965, pp. A1133.

[25] Dirac, P. A., "Note on exchange phenomena in the Thomas atom," *Mathematical Proceedings of the Cambridge Philosophical Society*, Vol. 26, Cambridge Univ Press, 1930, pp. 376–385.

[26] Perdew, J. P. and Zunger, A., "Self-interaction correction to density-functional approximations for many-electron systems," *Phys. Rev. B*, Vol. 23, May 1981, pp. 5048–5079.

[27] Perdew, J. P. and Yue, W., "Accurate and simple density functional for the electronic exchange energy: Generalized gradient approximation," *Physical Review B*, Vol. 33, No. 12, 1986, pp. 8800.

[28] Wang, L.-W. and Teter, M. P., "Kinetic-energy functional of the electron density," *Physical Review B*, Vol. 45, No. 23, 1992, pp. 13196.

[29] Wang, Y. A., Govind, N., and Carter, E. A., "Orbital-free kinetic-energy density functionals with a density-dependent kernel," *Physical Review B*, Vol. 60, No. 24, 1999, pp. 16350.

[30] Zhou, B., Ligneres, V. L., and Carter, E. A., "Improving the orbital-free density functional theory description of covalent materials," *The Journal of chemical physics*, Vol. 122, 2005, pp. 044103.

[31] Thomas, L. H., "The calculation of atomic fields," *Mathematical Proceedings of the Cambridge Philosophical Society*, Vol. 23, Cambridge Univ Press, 1927, pp. 542–548.

[32] Fermi, E., "Un metodo statistico per la determinazione di alcune priorieta dell'atome," *Rend. Accad. Naz. Lincei*, Vol. 6, No. 602-607, 1927, pp. 32.

[33] Teller, E., "On the stability of molecules in the Thomas-Fermi theory," *Reviews of Modern Physics (US)*, Vol. 34, 1962.

[34] Lieb, E. H., "Thomas-Fermi and related theories of atoms and molecules," *Reviews of Modern Physics*, Vol. 53, No. 4, 1981, pp. 603.

[35] Balàzs, N. L., "Formation of stable molecules within the statistical theory of atoms," *Physical Review*, Vol. 156, No. 1, 1967, pp. 42.

[36] Lieb, E. H. and Simon, B., "The Thomas-Fermi theory of atoms, molecules and solids," *Advances in Mathematics*, Vol. 23, No. 1, 1977, pp. 22–116.

[37] Chan, G. K.-L., Cohen, A. J., and Handy, N. C., "Thomas–Fermi–Dirac–von Weizsäcker models in finite systems," *The Journal of Chemical Physics*, Vol. 114, 2001, pp. 631.

[38] Tomishima, Y. and Yonei, K., "Solution of the Thomas-Fermi-Dirac equation with a modified Weizsäcker correction," *J. Phys. Soc. Japan*, Vol. 21, 1966, pp. 142–153.

[39] Brack, M., Guet, C., and Hakansson, H.-B., "Selfconsistent semiclassical description of average nuclear bulk properties-a link between microscopic and macroscopic models," *Physics Reports*, Vol. 123, 1985, pp. 275–364.

[40] Lindhard, J., "On the properties of a gas of charged particles," *Kgl. Danske Videnskab. Selskab Mat.-Fys. Medd.*, Vol. 28, 1954.

[41] Perrot, F., "Hydrogen-hydrogen interaction in an electron gas," *Journal of Physics: Condensed Matter*, Vol. 6, No. 2, 1994, pp. 431.

[42] Wang, L.-W. and Teter, M. P., "Kinetic-energy functional of the electron density," *Physical Review B*, Vol. 45, No. 23, 1992, pp. 13196.

[43] Smargiassi, E. and Madden, P. A., "Orbital-free kinetic-energy functionals for first-principles molecular dynamics," *Physical Review B*, Vol. 49, No. 8, 1994, pp. 5220.

[44] Ho, G. S., Lignères, V. L., and Carter, E. A., "Introducing PROFESS: A new program for orbital-free density functional theory calculations," *Computer physics communications*, Vol. 179, No. 11, 2008, pp. 839–854.

[45] Ceperley, D. and Alder, B., "Exchange-correlation potential and energy for density-functional calculation," *Phys. Rev. Lett*, Vol. 45, 1980, pp. 567–581.

[46] Perdew, J. P., "Density-functional approximation for the correlation energy of the inhomogeneous electron gas," *Physical Review B*, Vol. 33, No. 12, 1986, pp. 8822.

[47] Garcıa-Cervera, C. J., "An efficient real space method for orbital-free density-functional theory," *Commun. Comput. Phys*, Vol. 2, 2007, pp. 334–357.

[48] Gavini, V., Knap, J., Bhattacharya, K., and Ortiz, M., "Non-periodic finite-element formulation of orbital-free density functional theory," *Journal of the Mechanics and Physics of Solids*, Vol. 55, No. 4, 2007, pp. 669–696.

[49] Motamarri, P., Iyer, M., Knap, J., and Gavini, V., "Higher-order adaptive finite-element methods for orbital-free density functional theory," *Journal of Computational Physics*, Vol. 231, No. 20, 2012, pp. 6596–6621.

[50] Hindmarsh, A. C. and Taylor, A. G., "PVODE and KINSOL: Parallel software for differential and nonlinear systems," Tech. rep., Lawrence Livermore National Lab., CA (United States), 1998.

[51] Balay, S., Brown, J., Buschelman, K., Eijkhout, V., Gropp, W., Kaushik, D., Knepley, M., McInnes, L. C., Smith, B., and Zhang, H., "PETSc Users Manual Revision 3.4," 2013.

[52] Goodwin, L., Needs, R., and Heine, V., "A pseudopotential total energy study of impurity-promoted intergranular embrittlement," *Journal of Physics: Condensed Matter*, Vol. 2, No. 2, 1990, pp. 351.

[53] Tadmor, E. B., Ortiz, M., and Phillips, R., "Quasicontinuum analysis of defects in solids," *Philosophical Magazine A*, Vol. 73, No. 6, 1996, pp. 1529–1563.

[54] Woodward, C. and Rao, S., "Flexible ab initio boundary conditions: simulating isolated dislocations in bcc Mo and Ta," *Physical review letters*, Vol. 88, No. 21, 2002, pp. 216402.

[55] Ortiz, M., Cuitino, A., Knap, J., and Koslowski, M., "Mixed Atomistic–Continuum Models of Material Behavior: The Art of Transcending Atomistics and Informing Continua," *Mrs Bulletin*, Vol. 26, No. 03, 2001, pp. 216–221.

[56] Knap, J. and Ortiz, M., "An analysis of the quasicontinuum method," *Journal of the Mechanics and Physics of Solids*, Vol. 49, No. 9, 2001, pp. 1899–1923.

[57] Iyer, M. and Gavini, V., "A field theoretical approach to the quasi-continuum method," *Journal of the Mechanics and Physics of Solids*, Vol. 59, No. 8, 2011, pp. 1506–1535.

[58] Iyer, M. and Gavini, V., "Atomic Relaxation with Configurational Forces," Unpublished notes.

[59] Ho, G., Ong, M. T., Caspersen, K. J., and Carter, E. A., "Energetics and kinetics of vacancy diffusion and aggregation in shocked aluminium via orbital-free density functional theory," *Physical Chemistry Chemical Physics*, Vol. 9, No. 36, 2007, pp. 4951–4966.

[60] Triftshäuser, W., "Positron trapping in solid and liquid metals," *Phys. Rev. B*, Vol. 12, Dec 1975, pp. 4634–4639.

[61] Meyers, M., Mishra, A., and Benson, D., *Progress in Materials Science*, Vol. 51, 2006, pp. 427 – 556.

[62] Uchic, M. D., Dimiduk, D. M., Florando, J. N., and Nix, W. D., "Sample Dimensions Influence Strength and Crystal Plasticity," *Science*, Vol. 305, 2004, pp. 986–989.

[63] Trinkle, D. R. and Woodward, C., "The Chemistry of Deformation: How Solutes Soften Pure Metals," *Science*, Vol. 310, No. 5754, 2005, pp. 1665–1667.

[64] Zhu, T., Li, J., Samanta, A., Kim, H. G., and Suresh, S., "Interfacial plasticity governs strain rate sensitivity and ductility in nanostructured metals," *Proc. Nat. Acad. Sci.*, Vol. 104, 2007, pp. 3031–3036.

[65] Leyson, G., Curtin, W., Hector, L., and Woodward, C., "Quantitative prediction of solute strengthening in aluminium alloys," *Nature Materials*, Vol. 9, 2010, pp. 750 – 755.

[66] Bulatov, V. V., Yip, S., and Argon, A. S., "Atomic Modes of Dislocation Mobility in Silicon," *Philos. Mag. A*, Vol. 72, 1995, pp. 453–496.

[67] Duesbery, M. and Vitek, V., "Plastic anisotropy in b.c.c. transition metals," *Acta Materialia*, Vol. 46, 1998, pp. 1481–1492.

[68] Lu, G., Kioussis, N., Bulatov, V. V., and Kaxiras, E., "Generalized-stacking-fault energy surface and dislocation properties of aluminum," *Phys. Rev. B*, Vol. 62, 2000, pp. 3099–3108.

[69] Kabir, M., Lau, T. T., Rodney, D., Yip, S., and Van Vliet, K. J., "Predicting Dislocation Climb and Creep from Explicit Atomistic Details," *Phys. Rev. Lett.*, Vol. 105, 2010, pp. 095501.

[70] Pollock, T. and Argon, A., "Creep resistance of CMSX-3 nickel base superalloy single crystals," *Acta Metallurgica et Materialia*, Vol. 40, 1992, pp. 1–30.

[71] Lu, G. and Kaxiras, E., *Phys. Rev. Lett.*, Vol. 89, 2002, pp. 105501.

[72] Yasi, J. A., Jr., L. G. H., and Trinkle, D. R., "First-principles data for solid-solution strengthening of magnesium: From geometry and chemistry to properties," *Acta Materialia*, Vol. 58, 2010, pp. 5704 – 5713.

[73] Hansen, N., "HallPetch relation and boundary strengthening," *Scripta Materialia*, Vol. 51, 2004, pp. 801–806.

[74] Greer, J. R. and Nix, W. D., "Nanoscale gold pillars strengthened through dislocation starvation," *Phys. Rev. B*, Vol. 73, 2006, pp. 245410.

[75] Rice, J. R., "Dislocation nucleation from a crack tip: An analysis based on the Peierls concept," *Journal of the Mechanics and Physics of Solids*, Vol. 40, 1992, pp. 239 – 271.

[76] Fleck, N., Muller, G., Ashby, M., and Hutchinson, J., "Strain gradient plasticity: Theory and experiment," *Acta Metallurgica et Materialia*, Vol. 42, 1994, pp. 475 – 487.

[77] Nix, W. D. and Gao, H., "Indentation size effects in crystalline materials: A law for strain gradient plasticity," *Journal of the Mechanics and Physics of Solids*, Vol. 46, 1998, pp. 411 – 425.

[78] Ghoniem, N. M., Tong, S.-H., and Sun, L. Z., "Parametric dislocation dynamics: A thermodynamics-based approach to investigations of mesoscopic plastic deformation," *Phys. Rev. B*, Vol. 61, 2000, pp. 913–927.

[79] Arsenlis, A. and Parks, D. M., "Modeling the evolution of crystallographic dislocation density in crystal plasticity," *Journal of the Mechanics and Physics of Solids*, Vol. 50, 2002, pp. 1979–2009.

[80] Gumbsch, P. and Daw, M. S., "Interface Stresses and their Effects on the Elastic Moduli of Metallic Multilayers," *Phys. Rev. B*, Vol. 44, 1991, pp. 3934–3938.

[81] Ismail-Beigi, S. and Arias, T. A., "*Ab Initio* Study of Screw Dislocations in Mo and Ta: A New Picture of Plasticity in bcc Transition Metals," *Phys. Rev. Lett.*, Vol. 84, 2000, pp. 1499–1502.

[82] Woodward, C., Trinkle, D. R., Hector, L. G., and Olmsted, D. L., "Prediction of Dislocation Cores in Aluminum from Density Functional Theory," *Phys. Rev. Lett.*, Vol. 100, 2008, pp. 045507.

[83] Frederiksen, S. L. and Jacobsen, K. W., "Density functional theory studies of screw dislocation core structures in bcc metals," *Philosophical Magazine*, Vol. 83, 2003, pp. 365–375.

[84]

[85] Bulatov, V. and Cai, W., *Computer simulations of dislocations*, Vol. 3, Oxford University Press, 2006.

[86] Gavini, V., "Role of Macroscopic Deformations in Energetics of Vacancies in Aluminum," *Phys. Rev. Lett.*, Vol. 101, 2008, pp. 205503.

[87] Frenkel, J., "The theory of the elastic limit and the solidity of crystal bodies," *Z Phys*, Vol. 37, 1926, pp. 572–609.

[88] Taylor, G. I., "Faults in a material which yields to shear stress while retaining its volume elasticity," *Proceedings of the Royal Society of London. Series A*, Vol. 145, No. 854, 1934, pp. 1–18.

[89] Polanyi, M., "Über eine Art Gitterstörung, die einen Kristall plastisch machen könnte," *Zeitschrift für Physik*, Vol. 89, No. 9-10, 1934, pp. 660–664.

[90] Hirsch, P., Horne, R., and Whelan, M., "LXVIII. Direct observations of the arrangement and motion of dislocations in aluminium," *Philosophical Magazine*, Vol. 1, No. 7, 1956, pp. 677–684.

[91] Höllerbauer, W. and Karnthaler, H., "Beitr. elektonenmicr," *Direktabb. Oberfl*, Vol. 14, 1981, pp. 361.

[92] Srinivasan, S., Liao, X., Baskes, M., McCabe, R., Zhao, Y., and Zhu, Y., "Compact and dissociated dislocations in aluminum: implications for deformation," *Physical review letters*, Vol. 94, No. 12, 2005, pp. 125502.

[93] Bulatov, V., Richmond, O., and Glazov, M., "An atomistic dislocation mechanism of pressure-dependent plastic flow in aluminum," *Acta materialia*, Vol. 47, No. 12, 1999, pp. 3507–3514.

[94] Gavini, V., "Role of the defect core in energetics of vacancies," *Proceedings of the Royal Society A: Mathematical, Physical and Engineering Science*, Vol. 465, No. 2110, 2009, pp. 3239–3266.

[95] Hirth, J. P. and Lothe, J., *Thoery of Dislocations*, McGraw-Hill, New York, 1968.

[96] Shin, I. and Carter, E. A., "Possible origin of the discrepancy in Peierls stresses of fcc metals: First-principles simulations of dislocation mobility in aluminum," *Phys. Rev. B*, Vol. 88, 2013, pp. 064106.

[97] Kuhlmann-Wilsdorf, D. and Wilsdorf, H., "On the behavior of thermal vacancies in pure aluminum," *Journal of Applied Physics*, Vol. 31, No. 3, 1960, pp. 516–525.

[98] Eyre, B. and Bartlett, A., "An electron microscope study of neutron irradiation damage in alpha-iron," *Philosophical Magazine*, Vol. 12, No. 116, 1965, pp. 261–272.

[99] Horton, L. and Farrell, K., "The temperature dependence of the damage microstructures in neutron-irradiated vanadium," *Journal of Nuclear Materials*, Vol. 122, No. 1, 1984, pp. 687–692.

[100] Sawan, M. E., Kulcinski, G. L., and Ghoniem, N. M., "Production and behavior of point defects in pulsed inertial confinement fusion reactors," *Journal of Nuclear Materials*, Vol. 103, 1981, pp. 109–113.

[101] Zinkle, S. J. and Ghoniem, N. M., "Prospects for accelerated development of high performance structural materials," *Journal of Nuclear Materials*, Vol. 417, No. 1, 2011, pp. 2–8.

[102] Trachenko, K. O., Dove, M. T., and Salje, E. K., "Atomistic modelling of radiation damage in zircon," *Journal of Physics: Condensed Matter*, Vol. 13, No. 9, 2001, pp. 1947.

[103] Han, S., Zepeda-Ruiz, L. A., Ackland, G. J., Car, R., and Srolovitz, D. J., "Interatomic potential for vanadium suitable for radiation damage simulations," *Journal of applied physics*, Vol. 93, No. 6, 2003, pp. 3328–3335.

[104] Robinson, M. T., "Basic physics of radiation damage production," *Journal of nuclear materials*, Vol. 216, 1994, pp. 1–28.

[105] Zhou, B., Wang, Y. A., and Carter, E. A., "Transferable local pseudopotentials derived via inversion of the Kohn-Sham equations in a bulk environment," *Physical Review B*, Vol. 69, No. 12, 2004, pp. 125109.

[106] Gavini, V., Bhattacharya, K., and Ortiz, M., "Vacancy clustering and prismatic dislocation loop formation in aluminum," *Physical Review B*, Vol. 76, No. 18, 2007, pp. 180101.